

Image reconstruction algorithms in radio interferometry: from handcrafted to learned denoisers

Matthieu Terris,^{1*} Arwa Dabbech,¹ Chao Tang,¹ Yves Wiaux¹

¹*Institute of Sensors, Signals and Systems, Heriot-Watt University, Edinburgh EH14 4AS, UK*

Accepted XXX. Received YYY; in original form ZZZ

ABSTRACT

We introduce a new class of iterative image reconstruction algorithms for radio interferometry, at the interface of convex optimization and deep learning, inspired by plug-and-play methods. The approach consists in learning a prior image model by training a deep neural network (DNN) as a denoiser, and substituting it for the handcrafted proximal regularization operator of an optimization algorithm. The proposed AIRI (“AI for Regularization in Radio-Interferometric Imaging”) framework, for imaging complex intensity structure with diffuse and faint emission, inherits the robustness and interpretability of optimization, and the learning power and speed of networks. Our approach relies on three steps. Firstly, we design a low dynamic range database for supervised training from optical intensity images. Secondly, we train a DNN denoiser with basic architecture ensuring positivity of the output image, at a noise level inferred from the signal-to-noise ratio of the data. We use either ℓ_2 or ℓ_1 training losses, enhanced with a nonexpansiveness term ensuring algorithm convergence, and including on-the-fly database dynamic range enhancement via exponentiation. Thirdly, we plug the learned denoiser into the forward-backward optimization algorithm, resulting in a simple iterative structure alternating a denoising step with a gradient-descent data-fidelity step. The resulting AIRI- ℓ_2 and AIRI- ℓ_1 were validated against CLEAN and optimization algorithms of the SARA family, propelled by the “average sparsity” proximal regularization operator. Simulation results show that these first AIRI incarnations are competitive in imaging quality with SARA and its unconstrained forward-backward-based version uSARA, while providing significant acceleration. CLEAN remains faster but offers lower reconstruction quality.

Key words: techniques: image processing – techniques: interferometric

1 INTRODUCTION

1.1 RI image formation challenge & CLEAN

Aperture synthesis by radio interferometry (RI) in astronomy probes the radio sky by measuring an incomplete coverage of the spatial Fourier domain of the image of interest, yielding an ill-posed inverse problem towards image formation. Modern and upcoming radio telescopes are designed to bring unprecedented resolution and sensitivity. In this context, the algorithms to be deployed to solve the inverse imaging problem face an ever increasing requirement to jointly deliver precision (*i.e.* high resolution and dynamic range), robustness (*i.e.* endowed with calibration and uncertainty quantification functionalities), and scalability (*i.e.* the capability to process sheer data volumes).

Most RI imaging pipelines utilized by astronomers are based on the CLEAN algorithm, originally proposed by Högbom (1974). Assuming a sparse sky model, the greedy algorithm proposes to iteratively remove the contribution of each point source in the dirty image (more generally known as backprojected image, defined as the inverse Fourier transform of the data). Numerous extensions of CLEAN have been devised over the last fifty years for acceleration purposes and

to generalize it to more complex emission structures, addressing not only intensity but also polarization imaging (*e.g.* Schwarz 1978; Schwab & Cotton 1983; Bhatnagar & Cornwell 2004; Cornwell et al. 2008; Thompson et al. 2017). Albeit simple and computationally efficient, CLEAN-based algorithms are known to provide a limited imaging quality when reconstructing diffuse emission with complex and faint structure across the field of view. Restored CLEAN images tend to exhibit artefacts due to the simplicity of the underlying prior image models. Their resolution is also limited to the spatial bandwidth of the observed data due to the convolution of the raw reconstruction with a smoothing beam, the so-called CLEAN beam. Restored intensity images are also affected by negative flux values due to the addition of residuals into the final solution. Not to mention that CLEAN reconstruction often requires some manual intervention.

1.2 State-of-art optimization algorithms & Bayesian inference

The field of convex and nonconvex optimization offers a powerful framework to solving inverse imaging problems. In this framework, a so-called objective function is defined, typically as the sum of a data-fidelity term and a regularization term injecting a prior image model to compensate for data incompleteness. The image estimate is defined as the minimizer of this objective and is reached via provably convergent algorithms. A celebrated class of algorithms from

* E-mail: m.terris@hw.ac.uk

this framework are the so-called proximal splitting methods (Combettes & Pesquet 2011), among which the Forward-Backward (FB) algorithm, alternating between a (forward) gradient-descent step enforcing data-fidelity and a (backward) proximal step enforcing the prior model via the application of the so-called proximal operator of the regularization term. The obtained solution can also be understood in a Bayesian framework as a *maximum a posteriori* (MAP) estimate with respect to a posterior distribution, the negative logarithm of which is the objective. The versatility of the convex optimization framework enables the use of sophisticated priors (such as hard constraints and other non-differentiable functions), which has progressively imposed convex optimization as a cornerstone of current state-of-the-art techniques in image reconstruction (Chambolle et al. 1998; Bonettini et al. 2008; Beck & Teboulle 2009; Chambolle & Pock 2011; Bredies & Holler 2020), of which medical imaging is a critical example (Lustig et al. 2007; Majumdar & Ward 2012; Bredies & Holler 2020; Ahmad et al. 2020). Since the advent of compressive sensing theory (Candès et al. 2006; Donoho 2006; Baraniuk 2007), sparsity priors have emerged strongly and have led to new approaches where one aims at enforcing sparsity of the sought signal in an appropriate domain, *e.g.* a wavelet or gradient domain (Mallat 1999; Lustig et al. 2007; Needell & Ward 2013; Poon 2015). In practice, these priors often translate within the reconstruction algorithm into simple thresholding-based proximal operators (Combettes & Wajs 2005; Combettes & Pesquet 2011). Since their first inception by Wiaux et al. (2009), convex and nonconvex optimization algorithms underpinned by sparsity priors have also emerged in RI imaging (Li et al. 2011; Dabbech et al. 2015; Garsden et al. 2015; Onose et al. 2016, 2017; Pratley et al. 2018). In particular, the Sparsity Averaging Reweighted Analysis (SARA) family of algorithms, developed for monochromatic intensity imaging (Carrillo et al. 2012, 2014; Onose et al. 2016, 2017; Pratley et al. 2018; Dabbech et al. 2018; Repetti et al. 2017), wideband intensity imaging (Abdulaziz et al. 2016, 2019; Thouvenin et al. 2021), and polarization imaging (Birdi et al. 2018; Birdi et al. 2020), lead to a much higher image precision than that offered by advanced versions of CLEAN, yet at the expense of a significant increase of the computational cost, ultimately affecting their scalability to large data volumes. Software associated with the SARA family can be found on the Puri-Psi webpage (Puri-Psi 2021).

Bayesian inference approaches have been proposed in the literature to address the RI image formation problem (Junklewitz et al. 2015; Arras et al. 2018; Cai et al. 2018; Arras et al. 2019). Although enabling uncertainty quantification of the obtained image estimate, this class of methods remains computationally very demanding for the data volumes expected by modern radio telescopes. This limitation triggered the development of an uncertainty quantification approach fully powered by optimization algorithms (Repetti et al. 2018, 2019).

1.3 Deep learning & first RI imaging applications

With the recent developments of deep learning, new techniques have emerged for solving image reconstruction problems in fields such as medical imaging, where Deep Neural Networks (DNNs) were demonstrated offering outstanding reconstruction quality (Jin et al. 2017; Wang et al. 2018b; Ongie et al. 2020; Zhang et al. 2021). A first and straightforward technique leveraging deep learning consists in training a DNN in a supervised manner to take observed data as an input (typical in an image format, as RI’s dirty image) and output an image estimate (Jin et al. 2017; Guan et al. 2019; Zhang et al. 2019a; Muckley et al. 2021). The training relies on a database of input and target (groundtruth) output images. Whatever the spe-

cific choice of DNN architecture, the parameters of all the layers are learned to minimize a training loss, typically the average distance between input and output over the database, by leveraging stochastic optimization algorithms such as Adam (Kingma & Ba 2015). Training is computationally very expensive and relies on dedicated hardware such as GPUs but, once the DNN is trained, an image estimate can be obtained by simply applying the DNN to a dataset of interest. The reconstruction is non-iterative and can be extremely fast when launched on GPU in comparison with optimization algorithms. This comes despite the fact that the layers of a DNN can be compared to the iterations of an optimization algorithm, as they come in finite, and often very small, number (Gregor & LeCun 2010; Jin et al. 2017). This analogy in fact triggered a very active line of research consisting in designing DNN architectures resulting from unfolding the iterations of optimization algorithms (Adler & Öktem 2018; Bertocchi et al. 2020).

Note that in this supervised setting, the DNN is trained for a specific image reconstruction task which is strongly tied to the training database, and in particular, to the measurement operator used to create the degraded observations. DNNs are known to be subject to robustness issues (Ian J Goodfellow & Szegedy 2015; Nguyen et al. 2015; Pang et al. 2018). Their exploitation raises questions, not only with regards to the interpretability of the obtained solution, specifically in a Bayesian context, but also their generalizability, *i.e.* their ability to provide accurate reconstruction quality in the case of acquisition conditions unseen during training. In RI imaging, the details of the acquisition, in particular the image dimension, the spatial Fourier coverage, and other instrumental and atmospheric effects, are very observation-dependent and not controllable. The generalizability issue is thus very acute in this context.

A second technique leveraging DNNs consists in preprocessing the data with a robust imaging approach, followed by the application of a DNN as a postprocessing step (Zhang et al. 2018; Bertocchi et al. 2020; Terris et al. 2021). Such an approach can at least partially solve the generalizability question by making the task of the DNN simpler. Few recent works have contemplated the use of DNNs for end-to-end reconstruction or postprocessing in RI imaging. In Terris et al. (2019), we proposed a deep postprocessing approach consisting in using a simple and fast optimization algorithm for preprocessing, before applying a DNN for artefacts removal. To keep preprocessing fast, the optimization algorithm should rely on simple regularization and not be run to full convergence, aiming to remove dependency to the details of the measurement operator, but unavoidably introducing artefacts associated with the basic regularization. The role of the postprocessing DNN is therefore to remove the resulting artefacts. The approach was benchmarked against SARA, showing similar reconstruction quality in a fraction of the time, but on simplistic simulations only. Gheller & Vazza (2021) proposed an auto-encoder architecture trained to recover the groundtruth image either from the dirty image, or from a preprocessed version of the RI measurements obtained using CLEAN. The results have shown an improvement over the dirty image on simulations involving extended radio emission. The reconstructions are however affected by patching artefacts. Most recently, Connor et al. (2021) developed a DNN dubbed POLISH, showing promising results on simulations for a simple super-resolution task, also demonstrating an ability to perform end-to-end reconstruction on point-like sources from Very Large Array (VLA) observations.

In summary, beyond the generalizability and interpretability issues, these approaches have neither been thoroughly validated for high resolution high dynamic range imaging of complex structure involving diffuse and faint emission, nor compared with both CLEAN

and state-of-the-art optimization approaches. We note that [Sun & Bouman \(2020\)](#) proposed a variational Bayesian inference approach where the target posterior distribution is encapsulated in a generative DNN. The approach does not require any training data and enables efficient sampling of a probability distribution, and is thus capable of both estimation and uncertainty quantification. It was illustrated in RI imaging, but only for extremely limited image dimension.

1.4 Proposed hybrid plug-and-play framework

A third class of methods exploiting DNNs are the so-called plug-and-play (PnP) methods at the interface of deep learning and optimization theory ([Venkatakrishnan et al. 2013](#); [Chan et al. 2016](#); [Zhang et al. 2017, 2019b](#)). These methods offer a new versatile framework to design algorithms solving inverse imaging problems, inheriting simultaneously the robustness and interpretability of optimization approaches, and the learning power and speed of DNNs. The general approach consists in learning a prior image model by training a DNN as a denoiser and substituting it for the proximal regularization operator at the heart of an optimization algorithm for image reconstruction. Under an appropriate firm nonexpansiveness constraint on the denoiser, which basically requires that the denoising operator contracts distances, the resulting hybrid iterative algorithm can be proven to converge to a well-characterized solution. Importantly, as the DNN is trained as a denoiser on an image database to serve as a simple regularization operator, it is by construction applicable for any sensing procedure, *de facto* avoiding the generalization issue affecting end-to-end approaches. PnP algorithms have been shown to deliver outstanding image reconstructions in applications such as in image restoration ([Zhang et al. 2021](#)) and medical imaging ([Ahmad et al. 2020](#)). However, the denoiser often falls short from satisfying the convergence conditions, that is crucial when dealing with high precision imaging (e.g. radio images of high resolution and dynamic range) requiring a large number of iterations to reach convergence. Several methods have been proposed to ensure the firm nonexpansiveness of the denoiser ([Ryu et al. 2019](#); [Terris et al. 2020](#); [Hertrich et al. 2021](#)), yet often coming at the cost of either strong architectural constraints, or inaccurate control of the nonexpansiveness. In our recent work [Pesquet et al. \(2021\)](#), we proposed to augment the denoiser’s training loss with a firm nonexpansiveness term, in order to meet the PnP convergence conditions with no restrictions on the DNN architecture. We have also proposed a characterization of the PnP solution in the context of monotone operator theory, thus generalizing the MAP interpretation of the solution of pure optimization algorithms.

In this work, building on [Pesquet et al. \(2021\)](#), we introduce a PnP framework dubbed AIRI, standing for “AI for Regularization in Radio-Interferometric Imaging”. Focusing on monochromatic intensity imaging, our approach for developing a first AIRI algorithm capable of imaging complex structure with diffuse and faint emission can be summarized in three steps. The first step is to design, from publicly available optical images, a realistic but low dynamic range database of intensity images for supervised training. The second step is to train a DNN denoiser with basic architecture ensuring positivity of the reconstructed images, at the signal-to-noise ratio of the data. The training relies on a simple ℓ_2 or ℓ_1 loss enhanced with a firm nonexpansiveness term ensuring algorithm convergence, and on an on-the-fly exponentiation procedure for dynamic range enhancement. The third step resides in plugging the DNN into the FB optimization algorithm, resulting in a simple iterative structure alternating between a denoising step and a gradient-descent data-fidelity step. We finally validate the resulting AIRI- ℓ_2 and AIRI- ℓ_1

algorithms, implemented in Matlab, on high resolution high dynamic range simulations utilizing intensity images containing diffuse and faint emission across the field of view. Our test images are 3c353, Hercules A, Centaurus A, and Cygnus A, with sizes varying between 512×512 and 2176×2176 , and dynamic ranges between 10^4 and 10^5 . Our benchmark algorithms are (i) the multi-scale CLEAN version implemented in the C++ WSClean software package ([Offringa et al. 2014](#)), and (ii) two optimization algorithms from the SARA family leveraging the handcrafted “average sparsity” proximal regularization operator: SARA itself ([Onose et al. 2017](#)), and its unconstrained FB-based version uSARA that we introduce here. While SARA relies on an advanced primal-dual FB (PDFB) algorithm ([Pesquet & Repetti 2014](#)) enabling non-differentiable data-fidelity constraints, uSARA only differs from AIRI- ℓ_2 and AIRI- ℓ_1 by the use of the average sparsity proximal operator in lieu of a learned denoiser for regularization. It in fact corresponds to the standalone version of the imaging module of the joint calibration and imaging approach proposed in [Repetti et al. \(2017\)](#) and [Dabbech et al. \(2021\)](#). Results show that our first AIRI- ℓ_2 and AIRI- ℓ_1 are already, not only competitive with SARA and uSARA in terms of imaging quality, but also providing a significant acceleration. In a nutshell, AIRI does indeed inherit the robustness and interpretability of optimization approaches, and the learning power and speed of DNNs. The optimized C++ WSClean code remains significantly faster but CLEAN offers lower reconstruction quality.

The remainder of the paper is organized as follows. In Section 2, we review imaging approaches from proximal optimization, recall SARA, and introduce its unconstrained version uSARA. In Section 3, we review PnP algorithms through the prism of proximal algorithms and introduce AIRI. In Section 4, we study the performance of AIRI- ℓ_2 and AIRI- ℓ_1 through an extensive simulation setup, and in comparison with the benchmark algorithms. In Section 5, we draw our conclusions and discuss future work.

2 STATE-OF-ART OPTIMIZATION ALGORITHMS & RI

In this section, we firstly introduce the linear RI inverse problem for the reconstruction of monochromatic intensity images. We then introduce the class of proximal optimization algorithms at the core of numerous reconstruction methods in imaging sciences, with a strong emphasis on the simple FB algorithm. We finally provide a concise overview of the state-of-the-art SARA algorithm, and introduce its unconstrained version uSARA.

2.1 RI imaging problem

Aperture synthesis in RI probes the radio sky by measuring an incomplete coverage of the spatial Fourier domain of the image of interest, yielding an ill-posed inverse problem for image formation, more specifically, a deconvolution problem. Focusing on monochromatic intensity imaging and assuming a small field of view, each pair of antennas of a radio array acquires a noisy Fourier component of the intensity image to be formed, called a visibility. The associated Fourier mode (also called uv -point) is given by the projection of the corresponding baseline, expressed in units of the observation wavelength, onto the plane perpendicular to the line of sight ([Thompson et al. 2017](#)). The collection of the measured Fourier modes, accumulated during the observation, provides an incomplete coverage of the 2D Fourier plane (also called uv -plane) of the image of interest.

Considering a discrete formulation, and assuming a target intensity

image $\bar{x} \in \mathbb{R}^n$, the vector of visibilities $\mathbf{y} \in \mathbb{C}^m$ is related to the unknown image by (Carrillo et al. 2014; Onose et al. 2016)

$$\mathbf{y} = \Phi \bar{x} + e \quad \text{with } \Phi = \mathbf{G}\mathbf{F}\mathbf{Z}, \quad (1)$$

where $\mathbf{G} \in \mathbb{C}^{m \times d}$ is a non-uniform Fourier transform interpolation matrix, $\mathbf{F} \in \mathbb{C}^{d \times d}$ is the 2D Discrete Fourier Transform, $\mathbf{Z} \in \mathbb{R}^{d \times n}$ is a zero-padding operator incorporating the correction for the convolution performed through the operator \mathbf{G} , and $e \in \mathbb{C}^m$ is the realization of some i.i.d. Gaussian random noise, with zero mean and standard deviation $\tau > 0$. We note that, not only implementing \mathbf{F} with the Fast Fourier Transform (FFT), but also encoding \mathbf{G} as sparse matrix, are paramount to ensure a fast scalable implementation of the measurement operator (see Puri-Psi (2021)).

The representation of the data in the image domain is called the dirty image, more generally known as backprojected image, given by $\text{Re}\{\Phi^\dagger \mathbf{y}\}$, where $(\cdot)^\dagger$ denotes the complex conjugate transpose. Backprojecting problem (1) into the image domain in fact gives

$$\text{Re}\{\Phi^\dagger \mathbf{y}\} = \text{Re}\{\Phi^\dagger \Phi\} \bar{x} + \text{Re}\{\Phi^\dagger e\}, \quad (2)$$

where $\text{Re}\{\Phi^\dagger \Phi\}$ is the operator representing the convolution of \bar{x} by the point spread function, also known as the dirty beam, and $\text{Re}\{\Phi^\dagger e\}$ is the noise backprojected in the image domain.

We add two remarks with regards to the generality of the measurement model formulation. Firstly, the dynamic range of interest for current and future observations requires taking into account the direction-dependent effects (DDEs) of atmospheric or instrumental origins, thus complicating the RI measurement operator. More precisely, each visibility is formed from the modulation of the radio image with the product of the DDE patterns specific to associated antenna and time instant. The DDEs are typically unknown and need to be calibrated, leading to a blind deconvolution imaging problem, which requires the design of joint calibration and imaging approaches, typically alternating between imaging and calibration modules (Repetti et al. 2017; Dabbech et al. 2021). One exception to this, is the so-called w -term induced by the projection of the baseline associated with each visibility on the line of sight, which becomes non-negligible on wide fields of view, and thus acts as a known DDE. In practice, DDEs can be integrated into extended convolution kernels in \mathbf{G} (Thouvenin et al. 2021). In this work, we assume a measurement operator Φ not affected by any known or unknown DDE, considering a pure imaging problem on small fields of view.

Secondly, the measurement model (1) assumes noise with constant variance across visibilities. In full generality, the noise is not white, and a diagonal whitening matrix $\Theta \in \mathbb{R}^{m \times m}$ with entries equal to the inverse noise standard deviation per visibility can be applied to the original measurement vector, ensuring that the resulting visibility vector is indeed affected by white noise. In this case problem (1) still holds, with a measurement operator $\Phi = \Theta \mathbf{G}\mathbf{F}\mathbf{Z}$, and \mathbf{y} and e the visibility and noise vectors after application of the whitening matrix. This operation is known as natural weighting. This scheme is used by the algorithms of the SARA family to ensure the negative log-likelihood interpretation of its data-fidelity terms (Carrillo et al. 2012). More complex weighting schemes, such as uniform and Briggs weighting, are used by CLEAN (Briggs 1995), which involve additional multiplicative terms in Θ . Both approaches add to natural weighting by downweighting visibilities in regions of the uv -plane with high sampling density, with the aim to reduce the sidelobes of the dirty beam and improve the resolution of the CLEAN reconstruction, though at the expense of sensitivity. Interestingly, Onose et al. (2017) showed for algorithms of the SARA family specifically that, while keeping to natural weighting, using sampling density information in acceleration strategies such as preconditioning are very

efficient at bringing jointly optimal resolution and dynamic range. In other words, the resolution-versus-sensitivity trade-off disappears asymptotically at convergence.

In this work, without loss of generality, our simulations consider i.i.d. Gaussian random measurement noise so that $\Theta = \mathbf{I}$ for natural weighting, where \mathbf{I} denotes the identity matrix. All algorithms discussed (SARA, uSARA, AIRI) use natural weighting, aside from CLEAN, which will be implemented with uniform weighting (see Section 4.1.2).

2.2 Proximal algorithms & FB

Leaving the nature of Φ aside, problems of the likes of (1) are ubiquitous in imaging sciences, and arise for instance in image restoration (Levin et al. 2009; Yang et al. 2010; Bredies & Holler 2020), hyperspectral imaging (Wang et al. 2015; Xie et al. 2019) and medical imaging (Gupta et al. 2018; Zbontar et al. 2018; Fessler 2020) to name a few. A widespread strategy to solve such a problem is to reformulate it as a convex minimization problem

$$\underset{\mathbf{x} \in \mathbb{R}^n}{\text{minimize}} f(\mathbf{x}) + \lambda r(\mathbf{x}), \quad (3)$$

where $f(\mathbf{x}) + \lambda r(\mathbf{x})$ is called the objective function, $f \in \Gamma_0(\mathbb{R}^n)$ ¹ is the term enforcing data-fidelity, and $r \in \Gamma_0(\mathbb{R}^n)$ is the regularization term introduced to compensate for the ill-posedness of (1) by enforcing a prior image model.

The theory of optimization offers a myriad of algorithms to solve such minimization problems, ranging from the simple FB algorithm (Bauschke & Combettes 2017), applicable if one of the two terms is differentiable, to ADMM (Boyd et al. 2011), or the Douglas-Rachford algorithm (Eckstein & Bertsekas 1992), applicable even if both f and r are non-differentiable, and more evolved structures, such as PDFB (Pesquet & Repetti 2014), that can handle multi-term objective functions with as many non-differentiable data-fidelity and regularization terms processed in parallel. All these algorithms are part of the same class of so-called proximal algorithms, in which context differentiable terms are optimized via gradient steps, while non-differentiable terms are optimized via their so-called proximal operator.

The proximal operator prox_r of a function $r \in \Gamma_0(\mathbb{R}^n)$ is defined as

$$(\forall \mathbf{z} \in \mathbb{R}^n), \quad \text{prox}_r(\mathbf{z}) = \underset{\mathbf{u} \in \mathbb{R}^n}{\text{argmin}} \frac{1}{2} \|\mathbf{z} - \mathbf{u}\|^2 + r(\mathbf{u}), \quad (4)$$

and can be interpreted as a generalization of the projection operator, or, interestingly, as a denoising operator. Indeed, problem (4) can be interpreted as the minimization problem to be solved for a simple denoising problem $\mathbf{z} = \mathbf{u} + \mathbf{w}$ where the data \mathbf{z} result from adding some i.i.d. Gaussian noise \mathbf{w} to the unknown \mathbf{u} . From this perspective, the first term of the objective function in (4) would be the standard data-fidelity term for denoising and r the regularization term. A proximal operator is a denoiser!

The choice of f and r in (3) is of paramount importance as it influences the final solution to the minimization task (Mallat 1999; Selesnick et al. 2005; Bredies & Holler 2020). Interpreting the reconstructed image as a MAP estimate leads naturally to choosing f as the negative log-likelihood associated with a given statistical model of the noise (typically a squared ℓ_2 norm for i.i.d. additive Gaussian noise), and r as the negative logarithm associated with a statistical

¹ $\Gamma_0(\mathbb{R}^n)$ denotes the set of convex, proper and lower-semicontinuous functions from \mathbb{R}^n to $(-\infty, \infty]$.

prior image model (typically, ℓ_1 norm for a Laplace prior). However, optimization algorithms are not tied to this statistical interpretation. In the context of compressive sensing theory (Candès et al. 2006; Donoho 2006; Baraniuk 2007), where sparsity is the postulated signal model, the choice of the ℓ_1 norm as a regularization term simply emanates from it being the closest convex relaxation of the natural sparsity measure that is the ℓ_0 norm. ℓ_1 regularization was shown to yield state-of-the-art image reconstruction methods beyond the context of compressive sensing. For instance, sparsity of the gradient is enforced as the ℓ_1 norm of the magnitude of the image gradient, that is the so-called Total Variation semi-norm (TV) (Rudin et al. 1992; Bredies et al. 2010; Bredies & Holler 2020), whereas sparsity of the sought image in a sparsifying domain $\mathbf{A} \in \mathbb{R}^{n \times p}$ can be enforced by choosing $r(\mathbf{x}) = \|\mathbf{A}^\dagger \mathbf{x}\|_1$ where \mathbf{A} can be a wavelet dictionary (Mallat 1999), an x-let transform (Candès & Demanet 2003; Do & Vetterli 2003), or a learned dictionary (Mairal et al. 2009), to name a few. Generally, the choice of the data-fidelity term is often driven by the statistical nature of the measurement noise, while regularization terms are carefully handcrafted to meet the specificities of the applications, with sparsity models defining the state-of-the-art. In summary, the MAP interpretation has its limitation, and in particular, setting the regularization parameter λ according to the proper normalization of the statistical models of which f and r would be the negative logarithms is known to often be suboptimal.

FB is the simplest of all proximal algorithms, typically applicable for $f, r \in \Gamma_0(\mathbb{R}^n)$, where f is differentiable. It is defined by the iterative sequence

$$(\forall k \in \mathbb{N}), \quad \mathbf{x}_{k+1} = \text{prox}_{\gamma \lambda r}(\mathbf{x}_k - \gamma \nabla f(\mathbf{x}_k)), \quad (5)$$

which is proven to converge towards a minimizer of the objective function (3), provided that $0 < \gamma < 2/L$ where L is the Lipschitz constant² of ∇f (Bauschke & Combettes 2017). Accelerated versions of FB also exist, leveraging inertial terms, preconditioning, and stochastic approaches. We also emphasize that FB can be used to solve problems involving nonconvex regularization terms r (Beck & Teboulle 2009; Attouch et al. 2013; Chouzenoux et al. 2014; Combettes & Pesquet 2015; Repetti & Wiaux 2021).

2.3 SARA & uSARA

2.3.1 SARA

A state-of-the-art optimization-based imaging algorithm for RI is the SARA approach (Carrillo et al. 2012, 2014; Abdulaziz et al. 2016; Onose et al. 2016, 2017; Birdi et al. 2018; Pratley et al. 2018; Dabbech et al. 2018; Abdulaziz et al. 2019; Thouvenin et al. 2021). In its monochromatic intensity imaging version, SARA consists in solving the constrained minimization problem given by

$$\underset{\mathbf{x} \in \mathbb{R}^n}{\text{minimize}} \quad \iota_{\mathcal{B}(\mathbf{y}, \epsilon)}(\Phi \mathbf{x}) + \lambda r(\mathbf{x}), \quad (6)$$

where $\iota_{\mathcal{B}(\mathbf{y}, \epsilon)}$ is the indicator function³ of the ℓ_2 -ball $\mathcal{B}(\mathbf{y}, \epsilon)$, that is centred at the data \mathbf{y} , of radius $\epsilon > 0$, and given by $\mathcal{B}(\mathbf{y}, \epsilon) = \{\mathbf{u} \in \mathbb{C}^m \mid \|\mathbf{y} - \mathbf{u}\| \leq \epsilon\}$. The ℓ_2 -bound ϵ is derived from the assumed i.i.d. Gaussian random noise statistics and is given by $\epsilon^2 = (2m + 4\sqrt{m})\tau^2/2$ (Carrillo et al. 2012). The function r defines

the SARA prior, also called the “average sparsity” prior, which consists of a positivity constraint and a log-sum prior promoting average sparsity in an over-complete dictionary $\Psi \in \mathbb{R}^{n \times bn}$. The dictionary Ψ is defined as the concatenation of $b = 9$ orthonormal bases (first eight Daubechies wavelets and the Dirac basis), re-normalized by $\sqrt{b} = 3$ to ensure that $\Psi\Psi^\dagger = \mathbf{I}$. From this, the prior r reads

$$r(\mathbf{x}) = \rho \sum_{j=1}^{bn} \log \left(\rho^{-1} \left| \left(\Psi^\dagger \mathbf{x} \right)_j \right| + 1 \right) + \iota_{\mathbb{R}_+^n}(\mathbf{x}), \quad (7)$$

where $(\cdot)_j$ denotes the j^{th} coefficient of its argument vector. The parameter $\lambda > 0$ is a regularization parameter. The parameter $\rho > 0$ is used to avoid reaching zero values in the argument of the log term. According to Thouvenin et al. (2021), both parameters should be set equal to an estimate of the standard deviation of the measurement noise in the wavelet domain.

Minimizing (6) should typically involve r via its proximal operator prox_r , dubbed the “average sparsity” proximal operator. In practice though, if the log-sum prior enforces a stronger sparsity in the solution than a typical ℓ_1 prior, it is also nonconvex. To address the resulting nonconvex minimization task, a reweighting procedure is adopted, where a sequence of convex surrogate minimization problems is solved iteratively (Candès et al. 2008; Carrillo et al. 2012), each involving a weighted- ℓ_1 prior g , given by

$$g(\mathbf{x}, \mathbf{W}) = \|\mathbf{W}\Psi^\dagger \mathbf{x}\|_1 + \iota_{\mathbb{R}_+^n}(\mathbf{x}), \quad (8)$$

where $\mathbf{W} \in \mathbb{R}^{bn \times bn}$ is a diagonal weighting matrix that needs to be updated after each resolution of the surrogate problem. The full SARA algorithm for solving (6) can be summarized as

$$\begin{aligned} & \text{for } i = 0, 1, \dots \\ & \quad \tilde{\mathbf{x}}_{i+1} = \underset{\mathbf{x} \in \mathbb{R}^n}{\text{argmin}} \quad \iota_{\mathcal{B}(\mathbf{y}, \epsilon)}(\Phi \mathbf{x}) + g(\mathbf{x}, \mathbf{W}_i) \\ & \quad \mathbf{W}_{i+1} = \text{Diag} \left(\rho \left/ \left(\rho + \Psi^\dagger \tilde{\mathbf{x}}_{i+1} \right) \right. \right), \end{aligned} \quad (9)$$

with $\mathbf{W}_0 = \mathbf{I}$, where $\text{Diag}(\cdot)$ denotes the diagonal matrix containing its (vector) argument on the diagonal. Minimizing each of these problems will now involve the weighted- ℓ_1 prior g via its proximal operator prox_g . One should acknowledge that the reweighting strategy also introduces significant complexity to the algorithm since a sequence of convex minimization problems needs to be solved.

Given the non-differentiability of the data-fidelity term in (6), the PDFB algorithm (Pesquet & Repetti 2014) is leveraged to solve each minimization task of the form (9). We note that because Ψ^\dagger is over-complete and due to the presence of the positivity constraint in (8), the proximal operator prox_g does not admit a closed-form solution, thus *a priori* requiring a sub-iterative structure. However, the full splitting functionalities of PDFB enable the decomposition of g into functions admitting simple proximal operators: a component-wise projection setting to zero imaginary parts and negative real parts, and a simple component-wise thresholding operation. These proximal operators are handled in parallel by PDFB without the need for sub-iterations (Onose et al. 2016). Interestingly, the same functionalities also enable handling large data volumes via parallel processing of data blocks (Onose et al. 2016), as well as large image sizes via parallel processing of image facets (Thouvenin et al. 2021), providing significant scalability to SARA.

2.3.2 Unconstrained SARA (uSARA)

Building on the works of Repetti & Wiaux (2021), we propose to focus on the unconstrained formulation of the SARA problem, that

² The Lipschitz constant of an operator $h : \mathbb{R}^n \rightarrow \mathbb{R}^p$ is defined as $\sup_{\mathbf{x} \neq \mathbf{y}} \|\mathbf{h}(\mathbf{x}) - \mathbf{h}(\mathbf{y})\| / \|\mathbf{x} - \mathbf{y}\|$.

³ The indicator function of a non-empty, closed, and convex set \mathcal{S} is defined as $\iota_{\mathcal{S}}(\mathbf{x}) = 0$ if $\mathbf{x} \in \mathcal{S}$, else $\iota_{\mathcal{S}}(\mathbf{x}) = +\infty$.

we dub unconstrained SARA (uSARA), again looked at from the prism of monochromatic intensity RI imaging only. More precisely, we consider the problem (3), with a differentiable data-fidelity term f chosen as the mean squared error loss, which corresponds to the negative log-likelihood of the data under the i.i.d. Gaussian random noise assumption, and is given by

$$f(\mathbf{x}) = \frac{1}{2} \|\Phi \mathbf{x} - \mathbf{y}\|^2. \quad (10)$$

Adopting the prior model r described in (7), the resulting nonconvex minimization task writes

$$\underset{\mathbf{x} \in \mathbb{R}^n}{\text{minimize}} \quad \frac{1}{2} \|\Phi \mathbf{x} - \mathbf{y}\|^2 + \lambda r(\mathbf{x}), \quad (11)$$

where $\lambda > 0$ is a regularization parameter. The nonconvexity of the prior r from (7) is handled through a similar reweighting procedure as in (9):

$$\begin{aligned} & \text{for } i = 0, 1, \dots \\ & \left[\begin{aligned} \tilde{\mathbf{x}}_{i+1} &= \underset{\mathbf{x} \in \mathbb{R}^n}{\text{argmin}} \quad \frac{1}{2} \|\Phi \mathbf{x} - \mathbf{y}\|^2 + g(\mathbf{x}, \mathbf{W}_i) \\ \mathbf{W}_{i+1} &= \text{Diag} \left(\rho \left/ \left(\rho + \Psi^\dagger \tilde{\mathbf{x}}_{i+1} \right) \right. \right), \end{aligned} \right. \end{aligned} \quad (12)$$

with $\mathbf{W}_0 = \mathbf{I}$. At each reweighting iteration, problem (12) can be solved with a standard FB algorithm. The full reweighting procedure for solving the uSARA problem (11) is summarized in Algorithm 1, where $\xi_1 > 0$ is a relative variation convergence criterion, and where the gradient of f at \mathbf{x} reads as

$$\nabla f(\mathbf{x}) = \text{Re}\{\Phi^\dagger \Phi\} \mathbf{x} - \text{Re}\{\Phi^\dagger \mathbf{y}\}, \quad (13)$$

and its Lipschitz constant is the spectral norm⁴ of $\text{Re}\{\Phi^\dagger \Phi\}$, i.e.

$$L = \|\text{Re}\{\Phi^\dagger \Phi\}\|. \quad (14)$$

Again, the stepsize γ needs to be upper-bounded by $2/L$.

As appears in the part of Algorithm 1 solving (12) (steps 5-7), the weighted- ℓ_1 prior g is involved via its proximal operator $\text{prox}_{\gamma \lambda g}$. The algorithmic structure does not exhibit the same full splitting functionalities as PDFB, and $\text{prox}_{\gamma \lambda g}$ must be computed iteratively. This can typically be achieved via a so-called dual FB algorithm (Combettes & Pesquet 2011), detailed in Algorithm 2, where $\xi_2 > 0$ is a relative variation convergence criterion. This algorithm alternates between a projection on the real positive orthant (Step 3), denoted by $\Pi_{\mathbb{R}_+^n}$, and the proximity operator of the dual of the weighted- ℓ_1 prior, which involves a component-wise soft-thresholding operator $\text{prox}_{\gamma \lambda \|\mathbf{W} \cdot\|_1}$ ⁵ (Step 4).

Formally Algorithm 1 and Algorithm 2 lead to a triply sub-iterative structure: a proximal operator loop (Step 2), inside a weighted- ℓ_1 loop (Step 5), inside a reweighting loop (Step 3). This suggests a possibly very computationally expensive algorithmic structure. However, firstly, Repetti & Wiaux (2021) have shown that only a fixed number of FB iterations K are required (Step 2), corresponding to the approximate minimization of (12), while preserving the convergence of the overall algorithm to a minimizer of the nonconvex objective (11). This is unlike SARA, where the sub-problems (9) need to be solved to convergence. The value of K can in fact be optimized to

⁴ The spectral norm of a linear operator is its maximum singular value, which can be computed via the power method (see e.g. Golub & Van Loan (2013)).

⁵ This operator, applied to \mathbf{z} boils down component-wise to $(\text{prox}_{\gamma \lambda \|\mathbf{W} \cdot\|_1}(\mathbf{z}))_j = \text{prox}_{\eta_j \cdot}(\mathbf{z}_j) = \text{sign}(\mathbf{z}_j) \max\{|\mathbf{z}_j| - \eta_j, 0\}$ where $\eta_j = \gamma \lambda \mathbf{W}_{j,j}$ is called the soft-thresholding parameter. All values below the threshold are set to 0 while those above are reduced by the value of the threshold (in absolute value).

Algorithm 1 Re-weighted FB algorithm for uSARA

```

1: given  $0 < \gamma < 2/L$ ,  $\lambda > 0$ ,  $\rho > 0$ ,  $\tilde{\mathbf{x}}_0 \in \mathbb{R}^n$ ,  $\xi_1 > 0$ 
2: Set  $\mathbf{W}_0 = \mathbf{I}$ 
3: repeat for  $i = 0, 1, \dots$ 
4:    $\mathbf{x}_0 = \tilde{\mathbf{x}}_i$ 
5:   repeat for  $k = 0, \dots, K$ 
6:      $\mathbf{x}_{k+1} = \text{prox}_{\gamma \lambda g}(\mathbf{x}_k - \gamma \nabla f(\mathbf{x}_k), \mathbf{W}_i)$ 
7:   end for
8:    $\tilde{\mathbf{x}}_{i+1} = \mathbf{x}_K$ 
9:    $\mathbf{W}_{i+1} = \text{Diag} \left( \rho \left/ \left( \rho + \Psi^\dagger \tilde{\mathbf{x}}_{i+1} \right) \right. \right)$ 
10: until  $\|\mathbf{x}_{K+1} - \mathbf{x}_K\| / \|\mathbf{x}_{K+1}\| < \xi_1$ 
11: return  $\tilde{\mathbf{x}}_{i+1}$ 

```

Algorithm 2 Dual FB algorithm for computing $\text{prox}_{\gamma \lambda g}(\mathbf{z}, \mathbf{W})$ in Algorithm 1

```

1: given  $\gamma > 0$ ,  $\lambda > 0$ ,  $\mathbf{W}$ ,  $\mathbf{z} \in \mathbb{R}^n$ ,  $\mathbf{v}_0 \in \text{Span}(\Psi^\dagger)$ ,  $\xi_2 > 0$ 
2: repeat for  $l = 0, 1, \dots$ 
3:    $\mathbf{x}_{l+1} = \Pi_{\mathbb{R}_+^n}(\mathbf{z} - \Psi \mathbf{v}_l)$ 
4:    $\mathbf{v}_{l+1} = \left( \mathbf{I} - \text{prox}_{\gamma \lambda \|\mathbf{W} \cdot\|_1} \right) \left( \mathbf{v}_l + \gamma \lambda \Psi^\dagger \mathbf{x}_{l+1} \right)$ 
5: until  $\|\mathbf{x}_{K+1} - \mathbf{x}_K\| / \|\mathbf{x}_{K+1}\| < \xi_2$ 
6: return  $\mathbf{x}_{l+1}$ 

```

provide significant acceleration of Algorithm 1, effectively removing one iteration layer. Secondly, the number of iterations in Algorithm 2 is moderate in practice when using an appropriate initialization strategy for the dual variable \mathbf{v}_0 , leading to mild computational cost of $\text{prox}_{\gamma \lambda g}$.

We conclude this section by underlining that uSARA corresponds to the imaging module of the joint calibration imaging approach described in Repetti et al. (2017) and Dabbech et al. (2021).

3 AIRI: AI FOR REGULARIZATION IN RI IMAGING

In this section, we introduce the proposed AIRI approach for monochromatic intensity imaging. After recalling the basics of the PnP framework in Section 3.1, Section 3.2 discusses convergence results of the PnP counterpart of uSARA under a firm nonexpansiveness constraint of the plugged denoiser, and the characterization of its solutions in the context of monotone operator theory. We then discuss in detail the proposed procedure to train the denoisers that will encapsulate our new RI image priors. In Section 3.3, we propose a methodology to estimate the training noise level from the signal-to-noise ratio of the data, which also sets the target dynamic range of the reconstruction. The section includes considerations to set the regularization parameter of uSARA, which plays a similar role to the training noise level in its PnP counterpart. In Section 3.4, we expose our approach to build a training database of images containing complex intensity structure with diffuse and faint emission, and a strategy for enhancing its dynamic range on-the-fly during training, to adapt to the specific dynamic range at which the denoiser is intended to operate. Section 3.5 details the specific training loss induced by these convergence, training noise level, and dynamic range enhancement considerations.

3.1 PnP-FB

When solving an inverse imaging problem from an optimization theory viewpoint, one defines an objective function, of which the sought image would be a minimizer and which can be obtained via an iterative algorithm. The PnP approach (Venkatakrishnan et al. 2013)

Algorithm 3 AIRI (PnP-FB) algorithm

```

1: given  $0 < \gamma < 2/L$ , denoiser  $D$ ,  $\mathbf{x}_0 \in \mathbb{R}^n$ ,  $\xi_3 > 0$ 
2: repeat for  $k = 0, 1, \dots$ 
3:    $\mathbf{x}_{k+1} = D(\mathbf{x}_k - \gamma \nabla f(\mathbf{x}_k))$ 
4: until  $\|\mathbf{x}_{k+1} - \mathbf{x}_k\| / \|\mathbf{x}_{k+1}\| < \xi_3$ 
5: return  $\mathbf{x}_{k+1}$ 

```

looks at the problem directly through the lens of the algorithm. As discussed in Section 2.2, it follows from the definition of a proximal operator that it can be interpreted as a denoiser. Borrowing a proximal optimization algorithm, the PnP approach proposes to replace the proximal regularization operator with a more general denoiser. More precisely, assuming a minimization problem of the form (3) with the differentiable data-fidelity term f , recall that the FB algorithm reads as in (5), with the proximal operator (4). Its PnP counterpart (PnP-FB) then simply follows as

$$(\forall k \in \mathbb{N}), \quad \mathbf{x}_{k+1} = D(\mathbf{x}_k - \gamma \nabla f(\mathbf{x}_k)), \quad (15)$$

where D is a denoising operator, *i.e.* an operator specifically designed to remove i.i.d. Gaussian random noise from an image.

Denoisers are ubiquitous in imaging sciences, and a large variety of denoisers have been defined and studied in the signal processing literature, including Gaussian filters, BM3D (Dabov et al. 2007), non local means (NLM) (Buades et al. 2011), with, more recently, deep neural networks (DNNs) leading the state of the art (Zhang et al. 2017). It is therefore very tempting to plug powerful denoisers in lieu of proximal operators... and play. In this context, we aim at taking advantage of the learning capabilities of DNNs in order to learn an appropriate regularization denoiser. Just as handcrafting the regularization term r (from which the proximal regularization operator prox_r results) is crucial to the reconstruction quality for a pure optimization approach, learning a powerful denoiser is cornerstone for the reconstruction quality of PnP algorithms. Recent advances in DNNs for image denoising tasks have shown new state of the art results over traditional denoisers (Zhang et al. 2017; Wang et al. 2018a; Zhou et al. 2020). Simultaneously, PnP algorithms with DNNs as denoisers have become the new state-of-the-art in image reconstruction (Zhang et al. 2021), significantly improving over their traditional optimization counterparts.

Yet, replacing the proximal operator with an off-the-shelf denoising operator is not inconsequential. In particular, a general non-proximal denoiser can *a priori* not be related with a regularization term in some overarching objective function. As a consequence, the characterization of the PnP solution (*e.g.* as a MAP estimator), and worse, the convergence properties of the iterative structure, are not ensured anymore, thus questioning the robustness and interpretability of PnP solutions. In order to secure the convergence of a PnP algorithm and the characterization of its solutions, a suggestion would be to ensure that the denoiser in (15) satisfies the same properties as a proximal operator. Unfortunately, this would be highly restrictive and difficult to enforce in practice. Several works have recently focused on restoring the convergence of PnP algorithms using DNN denoisers. The vast majority of these works ensure a nonexpansiveness constraint on the denoiser (Romano et al. 2017; Ryu et al. 2019; Cohen et al. 2021; Hertrich et al. 2021), but this constraint often comes with either restrictive assumptions on the algorithm, on the DNN architecture or on the operator ∇f .

3.2 Algorithm convergence and solution characterization

In Pesquet et al. (2021), casting the problem in the context of monotone operator theory, we have shown that the convergence of a PnP

algorithm can be ensured by introducing a well-chosen regularization in the training loss of the denoiser D enforcing firm nonexpansiveness without any form of limitation on the DNN architecture itself. Importantly, the approach also offers a generalized notion of characterization of its solution as solutions of monotone inclusion problems, generalizing pure optimization problems, hence opening a path towards generalizing the usual Bayesian MAP interpretation of optimization solutions. We summarize those results in the remainder of this section, as this is the framework in which AIRI is defined

Once again concentrating on a differentiable f such as (10), minimization problems like (3) can be reformulated (through their optimality conditions) as

$$\text{find } \hat{\mathbf{x}} \in \mathbb{R}^n \text{ s.t.} \quad 0 \in \nabla f(\hat{\mathbf{x}}) + \lambda \partial r(\hat{\mathbf{x}}), \quad (16)$$

where ∂r denotes the subdifferential⁶ of r . Problems as (16) are part of the class of so-called monotone inclusion problems and encompass unconstrained minimization problems such as uSARA (11). They can however take a more general flavour and write as

$$\text{find } \hat{\mathbf{x}} \in \mathbb{R}^n \text{ s.t.} \quad 0 \in \nabla f(\hat{\mathbf{x}}) + A(\hat{\mathbf{x}}), \quad (17)$$

where A is an operator satisfying some maximal monotonicity assumptions (Bauschke & Combettes 2017). It is important to stress that this class of operators includes, but is not restricted to, sub-differentials. Problem (17) is thus in general not equivalent to a minimization problem.

Solving such inclusion problems can be done using a generalized version of the proximal FB algorithm (5) with

$$(\forall k \in \mathbb{N}), \quad \mathbf{x}_{k+1} = J_{\gamma A}(\mathbf{x}_k - \gamma \nabla f(\mathbf{x}_k)), \quad (18)$$

where $J_{\gamma A}$ is the so-called resolvent of γA , yielding the convergence of the sequence $(\mathbf{x}_k)_{k \in \mathbb{N}}$ to $\hat{\mathbf{x}}$ satisfying (17). As previously, the stepsize γ must satisfy $0 < \gamma < 2/L$ where L is the Lipschitz constant of ∇f .

The resolvent operator can be seen as a generalized version of the proximal operator (4) (Bauschke & Combettes 2017). In fact, (5) is a special case of (18) since when $A = \lambda \partial r$ for $r \in \Gamma_0(\mathbb{R}^n)$, one has $J_{\gamma \lambda \partial r} = \text{prox}_{\gamma \lambda r}$. A key characterization of resolvent operators is the following: the operator J is the resolvent of a maximally monotone operator A if and only if it is firmly nonexpansive. Technically, by definition, an operator J is firmly nonexpansive if there exists an operator Q with Lipschitz constant smaller or equal to 1 such that $J = (I + Q)/2$, where I is the identity operator. Given the identical structure of PnP-FB and (18), it follows that D in (15) should be firmly nonexpansive for the convergence of the PnP algorithm to be ensured, with the PnP solutions characterized as solutions of a monotone inclusion problem (17). As resolvent operators are more general than proximal operators, this constraint is less restrictive than enforcing properties of a proximal operator on D . The PnP-FB algorithm with established convergence guarantees is summarized in Algorithm 3, where $\xi_3 > 0$ is a relative variation convergence criterion. In the RI imaging case of interest, we will define f as in (10), with the measurement operator Φ from (1). The gradient of f at \mathbf{x} therefore reads as in (13), with Lipschitz constant given in (14).

Finally, as already noted, the PnP-FB algorithm offers the basis for the direct PnP counterpart to uSARA, which is further discussed

⁶ The subdifferential of $r \in \Gamma_0(\mathbb{R}^n)$ is the set-valued operator defined as $\partial r(x) = \{u \in \mathbb{R}^n \mid (\forall z \in \mathbb{R}^n) \langle z - x, u \rangle + r(x) \leq r(z)\}$. When r is also differentiable, the subdifferential coincides with the gradient (*i.e.* $\partial r = \nabla r$), yet the subdifferential is also defined for nondifferentiable functions such as $\ell_{\mathcal{G}}(\mathbf{y}, \epsilon)$. We refer the reader to Bauschke & Combettes (2017) for more information.

in later sections. We also underline that a constrained minimization problem like SARA (6) can also be cast in the context of monotone inclusion problems, simply replacing ∇f with $\partial \iota_{\mathcal{B}(\mathbf{y}, \epsilon)}$ in (16). As a result, the PnP counterpart of an algorithm like SARA, solving a variant of (17) with ∇f replaced with $\partial \iota_{\mathcal{B}(\mathbf{y}, \epsilon)}$, can simply be obtained by plugging our firmly nonexpansive DNN denoiser into the Douglas-Rachford (Onose et al. 2016) or other primal-dual FB algorithm propelling SARA, in lieu of the average sparsity proximal operator associated with the regularization term (7).

3.3 Training noise level vs. uSARA regularization parameter

3.3.1 Denoising i.i.d. Gaussian noise of specific standard deviation

Building from Pesquet et al. (2021), our AIRI denoiser \mathbf{D} will be trained in a supervised approach to remove i.i.d. Gaussian random noise of specific standard deviation σ . In other words, \mathbf{D} is set to tackle the denoising problem

$$\mathbf{z} = \mathbf{u} + \sigma \mathbf{w}, \quad (19)$$

where \mathbf{z} denotes the noisy data input to the DNN, \mathbf{u} is the unknown image corresponding to the target output of the DNN, and $\mathbf{w} \sim \mathcal{N}(0, \mathbf{I})$. As discussed in next section, the input signal-to-noise ratio of the RI data provides a reliable handle on σ .

3.3.2 Equating training & target dynamic ranges

As already emphasized, for RI imaging, AIRI will emerge from PnP-FB with f from (10) and Φ from (1). We propose to set the training noise level σ for \mathbf{D} to an appropriate estimate of the standard deviation of some effective image-domain noise induced by the original i.i.d. Gaussian random noise of standard deviation τ on the Fourier data in (1). We propose below a procedure to estimate the standard deviation of this image-domain noise, which, for simplicity, we also approximate to be i.i.d. Gaussian random noise.

Firstly, we resort to the image-domain formulation (2) of (1), normalized by the Lipschitz constant L in (14): $\text{Re}\{\Phi^\dagger \mathbf{y}\}/L = \text{Re}\{\Phi^\dagger \Phi\} \bar{\mathbf{x}}/L + \text{Re}\{\Phi^\dagger \mathbf{e}\}/L$. By construction, the chosen normalization ensures that the convolution operator $\text{Re}\{\Phi^\dagger \Phi\}/L$ has unit spectral norm, so that the dirty image is at the same scale as the original image. The covariance matrix of the image-domain noise $\text{Re}\{\Phi^\dagger \mathbf{e}\}/L$ thus writes $\tau^2 \text{Re}\{\Phi^\dagger \Phi\}/2L^2$. Secondly, as proposed in Thouvenin et al. (2021), we discard the correlation structure of the image-domain noise via the approximation $\text{Re}\{\Phi^\dagger \Phi\} \simeq \mathbf{L}\mathbf{I}$, leading to a noise covariance matrix approximation $\tau^2 \mathbf{I}/2L$. As a result the effective image-domain noise is assumed i.i.d. Gaussian, and the original standard deviation τ in the measurement domain is rescaled to $\tau/\sqrt{2L}$ in the transfer to the image domain.

Equating the standard deviations of the training noise for \mathbf{D} and the image-domain noise leads to the following heuristic:

$$\sigma = \frac{\tau}{\sqrt{2L}}. \quad (20)$$

We note that this heuristic is algorithm agnostic, *i.e.* *a priori* independent of the algorithmic structure in which the denoiser is plugged. In this sense, while similar, it is simpler and more general than the one proposed in Pesquet et al. (2021), which was derived specifically by estimating σ around the fixed point of (15). As will be shown through simulations in Section 4, the proposed heuristic provides a very precise estimate of the optimal training noise level.

Assuming the validity of this heuristic, one must acknowledge a dependency of the AIRI training noise level σ on the measurement

model, via τ and L , thus possibly hinting at the same robustness question as for end-to-end approaches. However, this is a very degenerate dependency via a single scalar value, which can be circumvented by developing a one-dimensional shelf of denoisers for a large enough range of training noise values, and picking the appropriate denoiser satisfying (20) for PnP reconstruction.

We note that a training database will unavoidably exhibit a finite maximum peak signal value across a finite number of training images. Without loss of generality, we consider a normalized database of images whose maximum intensity values are lower or equal to 1 (see Section 3.4). Therefore, the generalizability of a trained denoiser to be used in a PnP framework for the reconstruction of images not satisfying this constraint cannot be ascertained. This apparent restriction can be solved trivially by rescaling the inverse problem (1) for the reconstruction of some $\bar{\mathbf{x}}$ from data \mathbf{y} , by an upper bound on the peak intensity in the image $\alpha \geq \max_j \{\bar{x}_j\}$, leading to the inverse problem

$$\frac{\mathbf{y}}{\alpha} = \Phi \left(\frac{\bar{\mathbf{x}}}{\alpha} \right) + \frac{\mathbf{e}}{\alpha}, \quad (21)$$

for a normalized image $\bar{\mathbf{x}}/\alpha$ peaking below 1. This problem can be solved using AIRI with denoiser noise level set according to the following update of the heuristic:

$$\sigma = \frac{\tau}{\alpha \sqrt{2L}}. \quad (22)$$

This simply shows that the dimension of σ is that of an inverse input image-domain peak signal-to-noise ratio rather than an absolute noise level, in line with the fact that the denoiser is trained on a normalized database. Furthermore, as the AIRI denoiser consistently categorizes σ -level values as noise to be removed, the input image-domain signal-to-noise ratio also naturally sets the target output signal-to-noise ratio or dynamic range of the reconstruction. In summary, our heuristic (22) simply stipulates that the training dynamic range σ^{-1} should be set equal to the target reconstruction dynamic range $\alpha \sqrt{2L}/\tau$.

In other words, a fully fledged AIRI package universally applicable for all RI measurement settings simply requires (i) training, once and for all, a one-dimensional σ -shelf of denoisers extending across the segment of possible dynamic ranges of interest, and (ii) simply picking the appropriate denoiser for PnP image reconstruction according to (22), with τ and α inferred from the visibility data, and solving the rescaled inverse problem (21).

We note that α only needs to be an upper bound, and given the span of maximum values in the training database, an order of magnitude of over-estimation (leading to a true peak after rescaling in (21) an order of magnitude below 1) can easily be accommodated without suffering from generalization issues. Such an upper bound can typically be inferred from the dirty image. Moreover, this flexibility on α in (21) and (22) can be used to adjust the target σ to that of an already trained denoiser. This, in turn, suggests that the σ -shelf of denoisers does not need to be highly sampled, but rather that a few denoisers can cover a large segment of dynamic ranges.

3.3.3 uSARA regularization parameter

We further note the very similar roles of the noise level σ of the regularization denoiser in PnP-FB and the regularization parameter λ in the FB algorithm (5) solving (3). At the level of the monotone inclusion problem, the operator \mathbf{A} in (17) in the PnP approach implicitly depends on σ as its resolvent \mathbf{D} does, while in the pure optimization approach, the operator \mathbf{A} explicitly depends on λ through $\mathbf{A} = \lambda \partial r$ (see (16)). At the algorithmic level, on the one hand, \mathbf{D} is a denoiser

and we have proposed to set σ to the estimate (20) of the effective image-domain noise level, or more generally to the inverse target reconstruction dynamic range value in (22). On the other hand, for the traditional FB algorithm, λ is involved in (5) via $\text{prox}_{\gamma\lambda r}$. Focusing on the specific uSARA instance described in Section 2.3.2, and summarized on Algorithms 1 and 2, $\gamma\lambda$ typically acts as a soft-thresholding parameter, thresholding out small values in the wavelet domain defined by the average sparsity dictionary. Setting its value to the standard deviation of the effective wavelet-domain noise, which according to Thouvenin et al. (2021) is the same as in the image domain given the unit spectral norm of the average sparsity dictionary Ψ , yields the heuristic:

$$\gamma\lambda = \frac{\tau}{\sqrt{2L}}. \quad (23)$$

We readily note that, in contrast with the reasoning leading to (20) and (22), the above reasoning for λ is specific to the FB structure underpinning uSARA. We also recall the parameter $\rho > 0$ in the definition of the average sparsity prior r in (7), used to avoid reaching zero values in the argument of the log term. This parameter represents a floor level for the wavelet coefficients (Carrillo et al. 2012; Thouvenin et al. 2021), and should naturally be set to the same effective wavelet-domain noise level estimate as λ : $\rho = \lambda$. We further note that a variation of the proposed heuristic for the wavelet-domain noise level arises from a slightly different approximation in the transfer of the noise level from the image domain to the wavelet domain. Instead of assuming noise level conservation due to the normalization of Ψ , one can analyze the noise in each of the 9 bases of the dictionary separately, discarding the noise correlation structure between each pair of bases. In this case, the orthonormality of each basis and its normalization by 3 suggests a correction factor 1/3 in the heuristic values: $\rho = \gamma\lambda \approx \tau/3\sqrt{2L}$.

As will be shown through simulations in Section 4, relation (23) indeed provides a very useful reference value to set λ in uSARA. Even though the 1/3 correction will be shown to bring a closer-to-optimal value, it is still not as precise an estimate as (22) is for the training noise level of AIRI denoisers. We emphasize that a significant body of work has been dedicated to the question of setting the regularization parameter in problems of the form (3), with no simple and accurate solution to our knowledge (Donoho & Johnstone 1995; Luisier et al. 2007; Vidal et al. 2020). In this context, the fact that (23) provides an appropriate reference value for λ in uSARA is an interesting result. However, the fact that the PnP-FB admits a very accurate heuristic to set the training noise level, enabling to remove the introduction of an arbitrary regularization parameter to be fine-tuned, represents a major advantage of AIRI over uSARA.

3.4 Training database with adaptive dynamic range

3.4.1 State-of-the-art and proposed approach

Supervised training of DNNs for imaging requires the definition of a database of images, which remains a main difficulty in translating deep learning methods to RI due to the absence of groundtruths. The few works that have leveraged deep learning techniques for RI imaging so far resorted to various approaches. In Terris et al. (2019), we used a high dynamic range simulated radio map from Bonaldi & Braun (2018) of size 32000×32000 containing mainly elliptical Gaussian sources, broken down into a database of 1100 images of size 512×512 . Gheller & Vazza (2021) relied on 1000 radio images of size 2000×2000 simulated with ENZO (Bryan et al. 2014) and augmented by random rotations, resulting in the appearance of realistic extended emission in the field of view. Connor et al. (2021)

generated a database of 900 synthetic images of size 2000×2000 containing elliptical Gaussian sources.

In this work, we are targeting high dynamic range imaging of complex structure with diffuse and faint emission across the field of view. The database to be designed for the training of the regularization denoiser thus needs to reflect this target. In that regard, we propose (i) to source publicly available optical astronomy images containing a rich combination of compact and diffuse emission, (ii) to preprocess these images, aiming to remove existing noise and artefacts via a preliminary denoising procedure, and (iii) to exponentiate their intensity values to create high dynamic range images. The procedure results in the creation of a rich and clean training database of 2235 training images of size 512×512 . More technical details are provided below.

3.4.2 Building a rich low dynamic range database

Firstly, we constituted a set of 32 large grayscale images $(\mathbf{u}_k^{\text{raw}})_{1 \leq k \leq 32}$ from optical astronomical intensity images available online⁷, containing complex structure with both compact and diffuse emission. Each image is normalized with maximum intensity value equal to 1, and when the image contained colour channels, those were averaged. The typical size of each of these images is 3500×3500 . The sample standard deviation of the residual noise in image regions with no signal, averaged over the 32 images reads $\sigma_0 \approx 1/64$, leading to a typical dynamic range of $\sigma_0^{-1} \approx 64$, orders of magnitude below the values of interest in modern RI observations.

Secondly, the images are preprocessed with the aim of removing the residual noise, which includes various compression artefacts, and would otherwise be learned as part of the image model during training. To that effect, for all $1 \leq k \leq 32$, a simple denoising problem is formulated for the recovery of a clean image $\bar{\mathbf{u}}_k$ from $\mathbf{u}_k^{\text{raw}}$: $\mathbf{u}_k^{\text{raw}} = \bar{\mathbf{u}}_k + \mathbf{e}_k$, assuming i.i.d. Gaussian random noise \mathbf{e}_k with standard deviation $\hat{\sigma}_k$. The denoising procedure applied consists in solving the optimization problem underpinning SARA in (6), with $\Phi = \mathbf{I}$ and $\mathbf{y} = \mathbf{u}_k^{\text{raw}}$, resulting in a denoised database $(\mathbf{u}_k^{\text{low}})_{1 \leq k \leq 32}$. We note that this procedure does not affect the (low) dynamic range of the images. In a nutshell, noise and artefacts are removed, but the floor signal level and maximum intensity remain essentially unchanged.

Finally, the cleaned images are split to create a rich and clean database $(\mathbf{u}_s^{\text{low}})_{1 \leq s \leq S}$ with $S = 2235$ images of size 512×512 ⁸ containing both compact and diffuse emission. The resulting images exhibit a whole distribution of maximum intensity values bounded by 1, and a corresponding distribution of dynamic range values, with $\sigma_0^{-1} \approx 64$ representing the “nominal” dynamic range value of the database.

3.4.3 Enhancing database dynamic range to target

In order to simulate the high dynamic range of interest in RI imaging, we propose to exponentiate pixel-wise the intensity value of all groundtruth images of the low dynamic range database. The exponentiation parameter will be set to achieve a final nominal dynamic range of the same order as the training dynamic range, which according to (22) is also equivalent to the target dynamic range of the reconstruction. Technically, the low dynamic range images $\mathbf{u}_s^{\text{low}}$ are

⁷ <https://noirlab.edu/public/images/>

⁸ When the image dimensions are not multiples of 512, a symmetric padding is used before splitting.

exponentiated through the following transform (understood pixel-wise):

$$\mathbf{u}_s = h(\mathbf{u}_s^{\text{low}}, a) = \frac{a^{\mathbf{u}_s^{\text{low}} - 1}}{a}, \quad (24)$$

for some parameter $a \gg 1$. Recalling that the maximum span of the pixel values in any $\mathbf{u}_s^{\text{low}}$ is $[\sigma_0, 1]$, the resulting maximum span of the exponentiated images is approximately $[a^{-1}(a^{\sigma_0} - 1), 1]$. The exponentiation thus preserves the database normalization with maximum intensity value across images bounded by 1, while providing control on the final nominal dynamic range $a(a^{\sigma_0} - 1)^{-1}$. Imposing this value to be equal to the training dynamic range leads to the following equation for a :

$$a = (1 + a\sigma)^{\sigma_0^{-1}}. \quad (25)$$

Parametrizing a as $a = b\sigma^{-1}$ leads to the following equation for the scaling factor b : $b = \sigma(1 + b)^{\sigma_0^{-1}}$. This equation can be solved numerically to estimate the exponentiation factor a as a function of σ_0 and σ . In summary, the high dynamic range groundtruth database $(\mathbf{u}_s)_{1 \leq s \leq S}$ results from the low dynamic range groundtruth database $(\mathbf{u}_s^{\text{low}})_{1 \leq s \leq S}$ via the exponentiation formula (24), with a set through (25).

Figure 1 summarizes the preprocessing pipeline for the creation of the low and high dynamic range databases. Notice the diversity of images in the training samples displayed in Figure 1 (c).

3.4.4 Generating noisy & groundtruth pairs on-the-fly

The supervised training approach considered relies on images pairs: the groundtruth images $(\mathbf{u}_s)_{1 \leq s \leq S}$ corresponding to the target outputs of the DNN, and the noisy images $(\mathbf{z}_s)_{1 \leq s \leq S}$ corresponding to the DNN input. Given our choice, described in Section 3.3.1, to build a denoiser tailored to tackle i.i.d. Gaussian random noise of specific standard deviation σ , the noisy high dynamic range images read

$$\mathbf{z}_s = \mathbf{u}_s + \sigma \mathbf{w}_s, \quad (26)$$

with $\mathbf{e}_s \sim \mathcal{N}(0, \mathbf{I})$ and σ given by (22).

Importantly, as the high dynamic range database of noisy and groundtruth pairs depends on the target dynamic range through (24) and (26), one version of the database would need to be computed and stored for each dynamic range of interest, which is a highly impractical and unnecessary approach. Instead \mathbf{z}_s and \mathbf{u}_s can simply be seen as functions of $\mathbf{u}_s^{\text{low}}$ and computed on the fly during training.

3.5 Training loss function

In this section, we discuss the definition of the training loss for supervised training of the DNN denoiser, and specifically how to enforce firm nonexpansiveness of D. From the discussion in Section 3.2, we know that it is sufficient that the denoiser D writes as $D = (I + Q)/2$, where Q has a Lipschitz constant smaller or equal to 1. Thus, defining $Q = 2D - I$, ensuring firm nonexpansiveness amounts to training D while ensuring that the Lipschitz constant of Q is less than 1, or equivalently, that its Jacobian satisfies $\|\nabla Q(\mathbf{x})\| \leq 1$ for all \mathbf{x} . We here note that enforcing rigorously Lipschitz constraints on DNNs is not trivial, and in fact, even computing the Lipschitz constant of a DNN is still today a difficult task (Scaman & Virmaux 2018). Yet, since most deep learning frameworks rely on Jacobian-vector products (Paszke et al. 2017; Balestrieri & Baraniuk 2021; Maddox et al. 2021), one can, given some \mathbf{x} , compute $\|\nabla Q(\mathbf{x})\|$ via the power

method. Thus, D would ideally be trained as a denoiser with a standard training loss, but under the constraint that $\|\nabla Q(\mathbf{x})\| \leq 1$ for all \mathbf{x} . As such a constraint is not trivial to impose in practice, and building on Pesquet et al. (2021), we propose to relax it and introduce a regularization term in the training loss that penalizes not firmly nonexpansive networks. Denoting $\theta \in \mathbb{R}^c$ the learnable parameters of D, the resulting training loss reads:

$$\underset{\theta \in \mathbb{R}^c}{\text{minimize}} \quad \frac{1}{S} \sum_{s=1}^S \left(\mathcal{L}(D_\theta(\mathbf{z}_s) - \mathbf{u}_s) + \kappa \max\{\|\nabla Q_\theta(\mathbf{z}_s)\|, 1 - \varepsilon\} \right), \quad (27)$$

with \mathbf{z}_s and \mathbf{u}_s given in (24) and (26) respectively, as functions of $\mathbf{u}_s^{\text{low}}$ computed on the fly during training. The second term in (27) is the nonexpansiveness regularization term, with $\kappa > 0$ the associated regularization parameter, and $\varepsilon > 0$ is a safety margin parameter. The first term \mathcal{L} is the standard part of the loss function, for which practical choices involve the ℓ_2 loss i.e. $\mathcal{L}(\cdot) = 1/2 \|\cdot\|^2$, and the ℓ_1 loss, i.e. $\mathcal{L}(\cdot) = \|\cdot\|_1$, which will both be studied in Section 4.

We emphasize that this penalty does not explicitly guarantee that the solution of this problem satisfies the constraint $\|\nabla Q(\mathbf{x})\| \leq 1$ on the database, where it is effectively evaluated, let alone for all \mathbf{x} . Various countermeasures are however deployed, which have been demonstrated to be effective at ensuring PnP convergence in practice (see Pesquet et al. (2021)). Firstly, the safety margin parameter $\varepsilon > 0$ is a mean to strengthen the penalty. Secondly, the term $\|\nabla Q\|$ is not computed exactly at \mathbf{y}_s , but instead at a point sampled uniformly at random on the segment $[\mathbf{z}_s, \mathbf{u}_s]$, with the aim to explore a richer set of images than those of the database only. Last but not least, the value of κ can, and should, be fine-tuned manually to optimize the balance between the regularization term and the standard loss \mathcal{L} .

4 SIMULATIONS AND RESULTS

In this section, we validate through simulations two first incarnations of the AIRI framework, namely AIRI- ℓ_2 and AIRI- ℓ_1 arising from ℓ_2 and ℓ_1 choices in the training loss (27), in comparison with SARA, uSARA, and CLEAN. Our RI simulations target monochromatic intensity imaging of complex structure with diffuse and faint emission. We firstly define our general simulation set up: the chosen high resolution high dynamic range test radio images, benchmark methods, evaluation metrics, as well as the chosen DnCNN DNN denoiser architecture and training particulars. We then demonstrate the effectiveness of the proposed approach through four experiments. Experiment 1 aims at assessing the quality of the AIRI- ℓ_2 and AIRI- ℓ_1 denoisers on a simple denoising problem, applied to 512×512 -sized image in comparison with the average sparsity proximal operator. Experiments 2 and 3 are conducted to assess the performance of AIRI- ℓ_2 and AIRI- ℓ_1 for RI image reconstruction on simulated data from uv -patterns of the MeerKAT telescope (Jonas et al. 2018), and 512×512 -sized images. More precisely, experiment 2 is focused on validating the heuristic (20) for optimized reconstruction quality with AIRI on several uv -patterns, while also investigating the optimal regularization parameter for uSARA. Experiment 3 provides a validation of AIRI across a wider variety of uv -patterns, studying its performance in terms of both image reconstruction quality and speed in comparison with SARA, uSARA, and CLEAN. Finally, experiment 4 utilizes a 2176×2176 -sized image of Cygnus A to push the validation to larger image scale and higher dynamic range, using a simulated acquisition with a VLA uv -pattern.

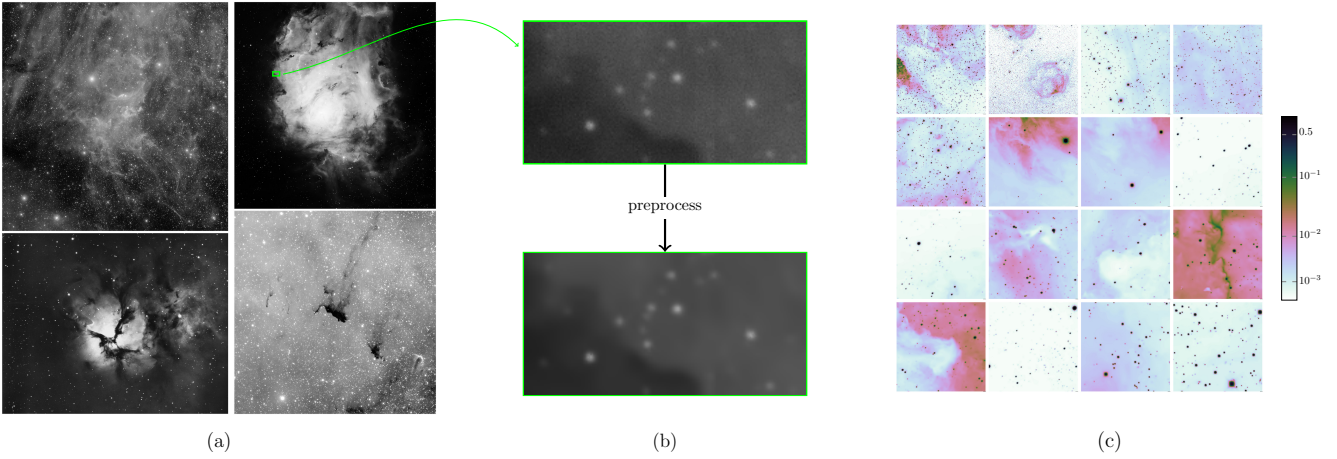


Figure 1. Summary of the proposed strategy for building a training database of postprocessed radio groundtruths. We first gather a set of 32 astronomical (optical) images of high quality but low dynamic range: (a) shows a subset of four images. (b) illustrates the effect of preprocessing on a small part of the image from (a). Eventually, we split the images into 2235 images of size 512×512 to create the low dynamic range training database. Samples of our training database, after application of the exponentiation (24) with $a = 10^3$, are shown in (c) in logarithmic scale.

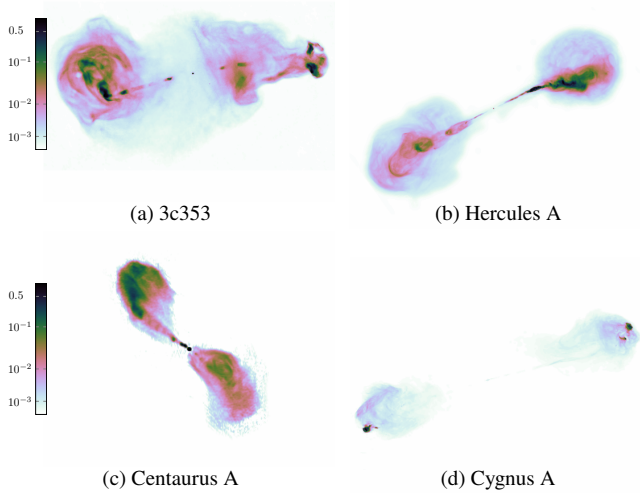


Figure 2. RI images of size $n = 512 \times 512$ considered as groundtruths to simulate the RI measurements in the first validation database (experiments 1-3), displayed in logarithmic scale.

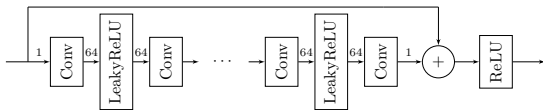


Figure 3. Architecture of the proposed denoising DNN, inspired from Zhang et al. (2017) and Pesquet et al. (2021), containing 20 convolutional layers in total. “Conv” denotes convolutional layers. The number of channels is given above the arrows. Notice the ReLU layer at the output, ensuring that our reconstructed RI images are positive.

4.1 Overall simulation set up

4.1.1 Test images

Our small test image database consists of two sets of RI images. The first set, shown in Figure 2, is composed of four radio images, namely 3c353, Hercules A, Centaurus A and Cygnus A, all resized to be of

size $n = 512 \times 512$ (see Figure 2). These images all have a peak value equal to 1 and dynamic ranges of approximately 2×10^4 for the three first images, and 10^5 for the latter. The simulations involving these images will target reconstruction dynamic ranges of the order of 10^4 . We note that this is already orders of magnitude higher than typical values in the PnP literature (Zhang et al. 2017, 2021; Pesquet et al. 2021), and therefore more challenging. The second test set consists of a single Cygnus A image of size $n = 2176 \times 2176$ from Dabbech et al. (2021), with peak value 0.922 and dynamic range 10^5 (see Figure 12). The simulations involving this image will also target more challenging dynamic range of reconstructions, of the order of 10^5 .

4.1.2 Benchmark methods

We benchmark our method with (i) uSARA (Algorithm 1) solving the unconstrained problem (11), (ii) SARA (Onose et al. 2017; Thouvenin et al. 2021), solving the constrained problem (6), and the multiscale variant of CLEAN implemented in the WSClean software (Offringa et al. 2014).

Regarding implementation details, we rely on the prescriptions of Thouvenin et al. (2021) for setting the hyperparameters of SARA. All simulations involving uSARA rely on a value for ρ using (23) including the $1/3$ correction factor, while the values of λ are fine-tuned around (23) to optimize the reconstruction quality. While AIRI- ℓ_2 , AIRI- ℓ_1 , uSARA, and SARA use natural weighting of the data, CLEAN is used with uniform weighting (see Section 2.1). Unlike optimization-based methods, the estimated model image of CLEAN is not physically realistic and is therefore smoothed with the CLEAN beam, to which the residual image is added. Consequently, the resolution of the resulting restored image is limited to the size of the CLEAN beam. Finally, note that the CLEAN restored image is in the units of Jansky per beam area, in contrast with SARA-based methods and AIRI, where the associated estimated images are in the units of Jansky per pixel. Therefore, in what follows, the reconstructed images with CLEAN are rescaled by the area of the CLEAN beam, for visualization purposes. Finally, we note that we always show the dirty image computed with a uniform weighing scheme, and rescaled in the $[0, 1]$ range for visualization purposes.

4.1.3 Evaluation metrics

For AIRI- ℓ_2 , AIRI- ℓ_1 , uSARA, and SARA, the image estimates $\hat{\mathbf{x}}$ are the reconstructed model images, while the image estimate considered for CLEAN is the restored image. The performance of all algorithms is assessed qualitatively via inspection of $\hat{\mathbf{x}}$, alongside the residual images, defined as $\hat{\mathbf{r}} = \beta \Phi^\dagger(\mathbf{y} - \Phi \hat{\mathbf{x}})$, where β is a normalization factor⁹. Given the high dynamic ranges of interest, the estimated images are shown in logarithmic scale, using the mapping $\text{rlog} = \mathbf{x} \mapsto \log_{10}(10^3 \mathbf{x} + 1)/3$. The residual images are displayed in linear scale.

We also consider two quantitative evaluation metrics, namely the SNR and logSNR of the estimated images $\hat{\mathbf{x}}$ with respect to the groundtruth $\bar{\mathbf{x}}$. The standard SNR metric (in dB) is defined as $\text{SNR}(\hat{\mathbf{x}}, \bar{\mathbf{x}}) = 20 \log_{10}(\|\bar{\mathbf{x}}\|/\|\bar{\mathbf{x}} - \hat{\mathbf{x}}\|)$. It simply corresponds to a logarithmic version of the norm of the error image $\bar{\mathbf{x}} - \hat{\mathbf{x}}$. The logSNR (in dB) is the SNR evaluated on a logarithmic version of the intensity images. This metric is introduced given the high dynamic ranges of interest, and assigns more relative weight to low intensities than the SNR. Our definition is $\text{logSNR}(\hat{\mathbf{x}}, \bar{\mathbf{x}}) = \text{SNR}(\text{rlog}(\hat{\mathbf{x}}), \text{rlog}(\bar{\mathbf{x}}))$.

4.1.4 DNN architecture & training particulars

Firstly, as highlighted already, the denoising losses that we use for \mathcal{L} in our training loss (27) are chosen to be either the ℓ_2 loss or the ℓ_1 loss, giving rise to AIRI- ℓ_2 and AIRI- ℓ_1 .

Secondly, we choose a basic DNN architecture for the denoiser \mathbf{D} , in the form of a modified DnCNN (Zhang et al. 2017) where the batch normalization layers have been removed, as in Pesquet et al. (2021). But in this work, a ReLU has been added as the last layer. This is a simple way to enforce positivity at the output of the denoiser, and therefore of the final reconstruction, much necessary as the developed AIRI algorithm targets intensity (versus polarization) imaging (see Figure 3).

Thirdly, the DNN is trained for 10^5 epochs with the Adam algorithm (Kingma & Ba 2015) and learning rate 10^{-4} , the learning rate being divided by 2 every 2000 epochs. $(\mathbf{z}_s, \mathbf{u}_s)$ in (27) are of size 46×46 , generated according to (26) and (24) from patches randomly extracted from the low dynamic range database of 512×512 images $(\mathbf{u}_s^{\text{low}})_{1 \leq s \leq S}$, itself augmented with random rotations and zooms. The Jacobian regularization in (27) is computed with a power method with a number of iterations increased to 10 in the later stages of the training to improve the precision of the computation. As observed in Pesquet et al. (2021), starting the optimization of the network from a pretrained state with $\kappa = 0$ in (27) enhances the results significantly.

Finally, we have observed that performing, at each iteration of the PnP algorithm, random flips and 90 degrees rotations of the image before applying the DNN, and inverting the transform after the denoising step, can significantly boost the reconstruction quality. We therefore adopt this strategy, inspired by the works of Zhang et al. (2021).

4.2 Experiment 1: validating the denoiser for denoising

4.2.1 Simulation setup

The PnP approach suggests that the best denoisers should provide the best regularizers. In this first experiment, we compare the denoising

⁹ The normalization factor is given by $\beta = 1/\max_i(\Phi^\dagger \Phi \delta)_i$, where δ is the image with value 1 at the phase centre and 0 otherwise. Hence, the dirty beam given by $\beta \Phi^\dagger \Phi \delta$, has a peak value equal to 1.

capabilities of the AIRI- ℓ_2 and AIRI- ℓ_1 denoisers on one side, and the average sparsity proximal operator propelling uSARA and SARA on the other side. To this end, we focus on a denoising problem

$$\mathbf{y} = \bar{\mathbf{x}} + \mathbf{e}, \quad (28)$$

where $\mathbf{y} \in \mathbb{R}^n$ is the data, $\bar{\mathbf{x}} \in \mathbb{R}^n$ is the groundtruth image, and $\mathbf{e} \in \mathbb{R}^n$ is the realization of an i.i.d. Gaussian random noise with zero mean and standard deviation τ . In other words, (28) is a degenerate case of problem (1) with $\Phi = \mathbf{I}$. We consider the 3c353 image as a groundtruth $\bar{\mathbf{x}}$. As already highlighted, the experiments involving 3c353 for the full validation of AIRI- ℓ_2 and AIRI- ℓ_1 , operate at a target dynamic range around 10^4 . We therefore design this preliminary pure denoising experiment with a similarly challenging target dynamic range and set the observation noise level to $\tau = 10^{-4}$.

Firstly, problem (28) can be solved using AIRI via Algorithm 3. As the image peaks at 1, $\alpha = 1$ and no rescaling of the inverse problem in (21) is needed. In this simple case, the gradient in (13) reads $\nabla f(\mathbf{x}) = \mathbf{x} - \mathbf{y}$ with Lipschitz constant in (14) $L = 1$. Taking $\gamma = 1/L = 1$, Algorithm 3 trivially boils down to a simple non-iterative application of \mathbf{D} to the data, leading to the denoised image

$$\hat{\mathbf{x}} = \mathbf{D}(\mathbf{y}). \quad (29)$$

The AIRI- ℓ_2 and AIRI- ℓ_1 denoisers were trained with a noise level $\sigma = \tau = 10^{-4}$ as per (22), on the proposed synthetic training database, and following the procedure explained in Section 3.5. Following the procedure detailed in Section 3.4.3, the corresponding exponentiation parameter for on-the-fly dynamic range enhancement of the database is $a \approx 10^3$. Furthermore, we set the regularization parameter in the training loss (27) to $\kappa = 10^{-9}$ and $\kappa = 10^{-5}$ for AIRI- ℓ_2 and AIRI- ℓ_1 denoisers respectively. The safety margin parameter is set to $\varepsilon = 5 \times 10^{-2}$. These values are chosen here as they are the ones to ensure the stability of Algorithm 3 in our next experiments.

Secondly, problem (28) can also be solved in a proximal approach with uSARA, setting $\Phi = \mathbf{I}$. Interestingly, in this case, the uSARA objective boils down to the objective defining the average sparsity proximal operator (see definition (4)) of λr , for the average sparsity prior r in (7), and $\lambda = \tau$ following the reasoning around equation (23). Therefore, applying Algorithm 1 results in computing the denoised image by simply applying the average sparsity proximal operator with appropriate λ :

$$\hat{\mathbf{x}} = \text{prox}_{\lambda r}(\mathbf{y}). \quad (30)$$

We note, given $\nabla f(\mathbf{x}) = \mathbf{x} - \mathbf{y}$ and $L = 1$, and further choosing $K = 1$ and $\gamma = 1/L = 1$, that Algorithm 1 greatly simplifies to the sequential application of $\text{prox}_{\gamma \lambda g}(\mathbf{y}, \mathbf{W}_i)$ with only the weights being updated at each iteration. The algorithm was run in this configuration, setting the convergence criteria to $\xi_1 = 6 \times 10^{-6}$ Algorithm 1, and $\xi_2 = 10^{-4}$ in Algorithm 2.

4.2.2 Experimental results

Denoising results are displayed in Figure 4. All three denoisers appear to be highly effective, both in terms of SNR and logSNR and visual denoising quality. The SNR values are very comparable. In terms of logSNR the AIRI- ℓ_1 denoiser achieves better performance than the AIRI- ℓ_2 denoiser, itself superior to the average sparsity proximal operator. Visually, the AIRI- ℓ_1 denoiser also achieves the reconstruction with the best resolution and least amount of artefacts (see zooms).

These results suggests that the AIRI- ℓ_1 and AIRI- ℓ_2 denoisers do

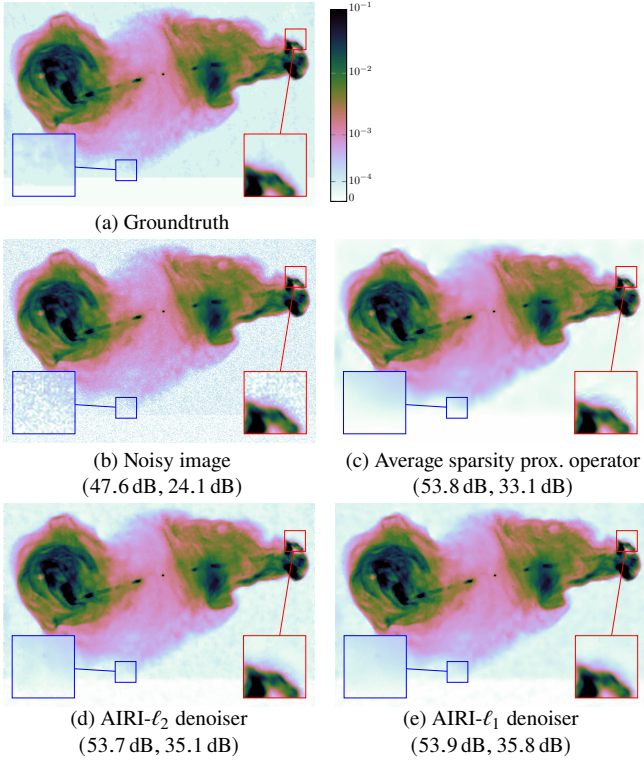


Figure 4. Experiment 1 results: Denoising results obtained with the proposed AIRI- ℓ_2 and AIRI- ℓ_1 denoisers in comparison with the averaged sparsity proximal operator. The respective groundtruth and noisy images are displayed in 4a and 4b. Denoising results obtained with the averaged sparsity proximal operator are shown in 4c, with AIRI- ℓ_2 in 4d and with AIRI- ℓ_1 in 4e. All images are displayed in logarithmic scale. The colourbar is saturated at 10^{-1} for clarity. Values of the obtained evaluation metrics (SNR, logSNR) are indicated below their associated images.

encapsulate a superior prior model to the average sparsity model encapsulated in the corresponding proximal operator.

4.3 Experiment 2: validating the training noise level heuristic

4.3.1 Simulation setup

Using our four 512×512 test images (see Figure 2), we study the impact of the noise level σ involved in the training of the AIRI- ℓ_2 and AIRI- ℓ_1 denoisers according to the procedure set in Section 3, and with the aim to validate the heuristic (22). We also study the optimal value of the regularization parameter λ of uSARA around the heuristic (23). The performance of AIRI- ℓ_2 and AIRI- ℓ_1 in terms of reconstruction quality is compared to that of uSARA.

We simulate RI observations utilizing simulated uv -coverages of the radio telescope MeerKAT. The uv -patterns correspond to five randomly selected pointing directions displayed in Figures 5 and 6c, and two of the four total observation durations displayed in Figure 6: $\Delta T \in \{4\text{ h}, 8\text{ h}\}$. The observed wavelength is 0.3m and the simulated sampling rate of the telescope is fixed to 100 points per hour. The data size thus increases linearly with ΔT . Data are simulated following the model described in (1), with input SNR defined as $\text{iSNR} = 20 \log_{10} (\|\Phi \bar{x}\|/\tau) = 30\text{ dB}$. We finally note that the uv -patterns extend to the edge of the considered Fourier domain as shown in Figures 5 and 6. In other words, we target mild, if any, super-resolution with respect to the nominal resolution of the observation, as set by the largest baseline.

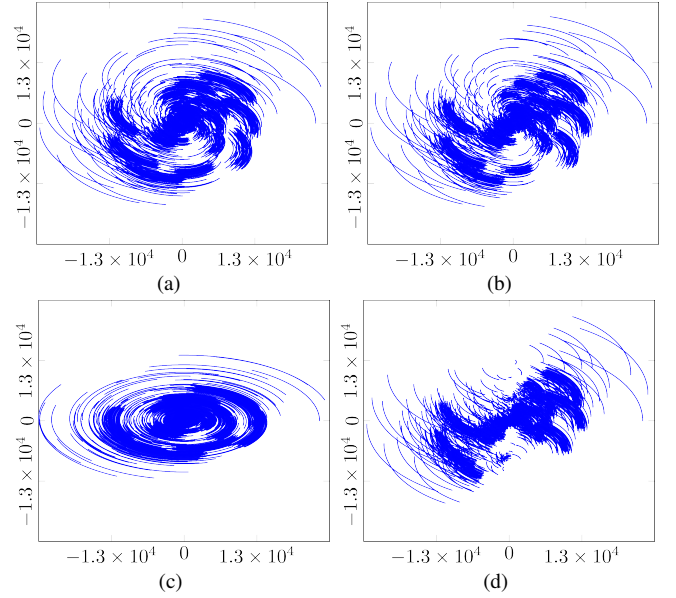


Figure 5. Experiments 1-3: MeerKAT uv -coverages simulated for four different telescope pointing directions and fixed total observation duration $\Delta T = 4\text{ h}$. The components are measured in units of the wavelength of the observation. Each uv -pattern contains $m = 806400$ points.

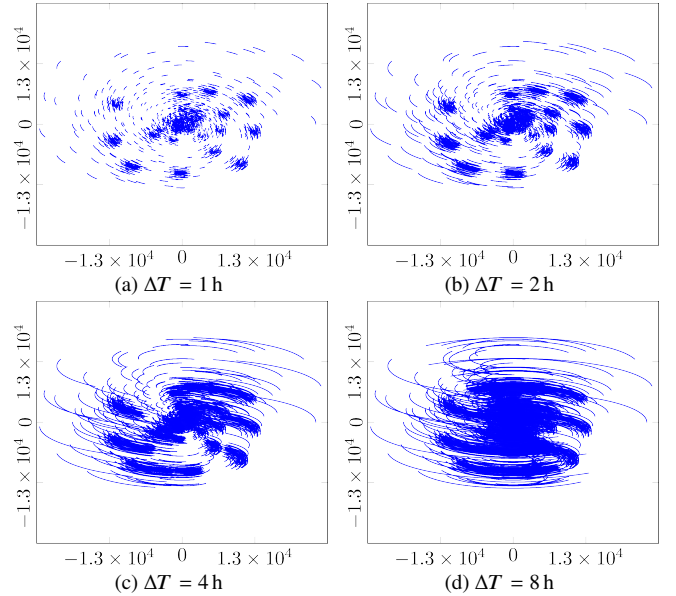


Figure 6. Experiments 1-3: MeerKAT uv -coverages associated with the four observation durations and fixed telescope pointing direction (complementary the four shown in Figure 5). The numbers of points in the uv -patterns are (a) $\Delta T = 1\text{ h}$: 201600, (b) $\Delta T = 2\text{ h}$: 403200, (c) $\Delta T = 4\text{ h}$: 806400, and (d) $\Delta T = 8\text{ h}$: 1612800.

Since our groundtruth images have peak values at 1 (*i.e.* $\alpha = 1$), a common heuristic value is reached for σ in (22) and $\gamma\lambda$ in (23). Obviously, τ and L are functions of Φ , and therefore of both the pointing direction and total duration of observation. However, the heuristic values are within a 25% variation range across pointing directions for each ΔT . For simplicity, a single heuristic value is considered for all five uv -patterns associated with the same ΔT , defined as $\nu_{\Delta T} \equiv \tau/\sqrt{2L}$, and taken to be the average of the values resulting for each pointing direction. The two resulting values are as announced associated with a target dynamic range around 10^4 : $\nu_4 = 1.4 \times 10^{-4}$ for $\Delta T = 4\text{ h}$, and $\nu_8 = 9 \times 10^{-5}$ for $\Delta T = 8\text{ h}$.

The values probed for $\gamma\lambda$ and σ are sampled a factor $\sqrt{2}$ around the heuristic and by steps of 2 thereafter.

Following the study by Pesquet et al. (2021), we choose the value of $\gamma = 1.98/L$ in Algorithms 1 and 3, which saturates the theoretical bound. The convergence criteria of Algorithms 1 and 3 are set to $\xi_1 = \xi_3 = 5 \times 10^{-6}$, with a maximum number of iterations of 6×10^3 , and we set $\xi_2 = 10^{-5}$ in Algorithm 2.

We train our AIRI- ℓ_2 and AIRI- ℓ_1 denoisers with optimized values $\kappa = 10^{-9}$ and $\kappa = 10^{-5}$ respectively in the training loss (27), with $\varepsilon = 5 \times 10^{-2}$, and observe that this ensures the stability of Algorithm 3 despite a spectral norm of the Jacobian slightly above 1. Following the procedure detailed in Section 3.4.3, the exponentiation parameter for on-the-fly dynamic range enhancement of the database is set to $a = 10^3$.

4.3.2 Experimental results

Considering the image of 3c353 as groundtruth and the uv -pattern from Figure 5a ($\Delta T = 4$ h) for simulating the measurements, reconstructions for different values of σ in AIRI- ℓ_2 and AIRI- ℓ_1 , and λ in uSARA are displayed in Figures 7 and 8. More precisely, model images, displayed in logarithmic scale, and their associated SNR and logSNR values are provided in Figure 7, and residual images are displayed in Figure 8 in linear scale. We firstly notice that σ and λ play a similar role in the reconstruction quality: the higher their value, the smoother the recovered image; the lower their value, the stronger the artefacts. Overall, reconstructions with uSARA exhibit some wavelet artefacts, particularly noticeable around bright compact sources overlaying faint extended emission. AIRI- ℓ_2 reconstructions typically exhibit less artefacts, but appear to be generally smoother. AIRI- ℓ_1 reconstructions contain even less artefacts, with an achieved resolution similar to uSARA. We conclude these observations by highlighting the low-amplitude residual images obtained with low values of σ and λ . However, such results are not a token of a good quality reconstruction. They instead reflect the over-fitting of the data in such settings.

Figure 9 shows the reconstruction SNR and logSNR graphs obtained when varying σ and $\gamma\lambda$ for reconstructions with AIRI and uSARA respectively, for both the total observation durations $\Delta T = 4$ h and $\Delta T = 8$ h. Each point on each of the four graphs gives the average value and 95% confidence interval over 20 reconstructions arising when considering the four test images in Figure 2 and five different pointing directions from Figures 5 and 6c.

Firstly, for both AIRI- ℓ_2 and AIRI- ℓ_1 , we observe that the SNR and logSNR metrics clearly peak at the proposed heuristic (22) (shown as the dashed vertical black line) for both $\Delta T = 4$ h and $\Delta T = 8$ h, suggesting that equating the training dynamic range to the target dynamic range is an accurate procedure. This result is also confirmed by the visual analysis in Figure 7. For uSARA, the SNR and logSNR results and the visual analysis in Figure 7 suggest that the relation (23) is a useful reference, but rather provides an upper-bound on the optimal value for the soft-thresholding parameter, roughly 6 to 11 times smaller when looked at from an SNR standpoint, or 3 to 6 times smaller from a logSNR perspective. In general, we find that the logSNR provides better coherence with the visual analysis, suggesting a optimal soft-thresholding value 3 to 6 times below the reference. Interestingly, the $1/3$ correction factor brings a closer-to-optimal value, but does not solve the discrepancy between the SNR and logSNR metrics. In contrast to AIRI- ℓ_2 and AIRI- ℓ_1 , uSARA thus exhibits an regularization parameter whose value cannot be set simultaneously automatically and optimally. This represents a significant advantage for the former over the latter.

Secondly, considering each method at its best, SNR and logSNR values for both $\Delta T = 4$ h and $\Delta T = 8$ h confirm a superior performance of AIRI- ℓ_1 over both AIRI- ℓ_2 and uSARA, the latter two achieving similar reconstruction qualities, with virtually same logSNR, and a slight SNR advantage for AIRI- ℓ_2 .

Thirdly, these results are in line with the visual analysis when considering each method at its best (see Figures 7d, 7i, 7m, and Figures 8b, 8g, 8k). AIRI- ℓ_2 and uSARA exhibit similar reconstruction qualities with the former smoother but with less artefacts than the latter. AIRI- ℓ_1 exhibits less artefacts than AIRI- ℓ_2 , while preserving the resolution offered by uSARA. AIRI- ℓ_1 provides the best residuals, uSARA residuals clearly contain sources discarded by the model and relating to the artefacts, while AIRI- ℓ_2 's higher residuals correlate with the sub-optimal resolution.

Fourthly, we recall that AIRI- ℓ_2 , AIRI- ℓ_1 , and uSARA are underpinned by the same FB algorithmic structure, and only differ by their choice of denoiser. From this perspective, the results of the current experiment are in line with those of the previous experiment, with a better regularization denoiser naturally leading to better overall reconstruction.

Finally, we observe that the confidence intervals around the mean SNR and logSNR values in Figure 9 are rather small for both AIRI- ℓ_2 and AIRI- ℓ_1 , and similar to those of uSARA. This is a first confirmation that in the PnP approach there is no issue of generalizability to measurement conditions not considered during training. This stems from the fact that the training of denoiser is by construction only very mildly sensitive to the measurement setting (through τ and L in (22) setting the training dynamic range equal to the input image-domain peak signal-to-noise ratio), in contrast with the case of end-to-end approaches (not investigated here) *a priori* sensitive to the details of the measurement model.

4.4 Experiment 3: validating AIRI in precision & cost

4.4.1 Simulation setup

In this section, we validate AIRI- ℓ_2 and AIRI- ℓ_1 more extensively, both in reconstruction quality and computational cost, across a wider range of observation durations, and in comparison with, not only uSARA, but also SARA and CLEAN. We consider the same four groundtruth images and experimental setup as for the previous experiment (see Section 4.3.1), with the same set of five pointing directions (see uv -coverages in Figures 5 and 6c). In order to further assess robustness to varying measurement conditions, the set of observation durations is enlarged to $\Delta T \in \{1 \text{ h}, 2 \text{ h}, 4 \text{ h}, 8 \text{ h}\}$ (see Figure 6).

We recall that our groundtruth images have peak values at 1, yielding the same heuristic value for σ and $\gamma\lambda$. These values are still within a 25% variation range across pointing directions for all four ΔT values, and a single heuristic value is considered for all five uv -patterns associated with the same ΔT . The resulting four average $v_{\Delta T} \equiv \tau/\sqrt{2L}$ are: $v_1 = 2.9 \times 10^{-4}$, $v_2 = 2.2 \times 10^{-4}$, $v_4 = 1.4 \times 10^{-4}$, and $v_8 = 9.3 \times 10^{-5}$. Given the result of the previous experiment the values of σ for AIRI- ℓ_2 and AIRI- ℓ_1 are taken exactly at the heuristic, while the value of $\gamma\lambda$ for uSARA is fine-tuned manually to optimize the logSNR of each reconstruction, again resulting in soft-thresholding values ranging between 3 and 6 times below the heuristic, depending on ΔT . Moreover, setting $\kappa = 10^{-9}$ (resp. $\kappa = 10^{-5}$) for the AIRI- ℓ_2 (resp. AIRI- ℓ_1) denoiser in (27), with $\varepsilon = 5 \times 10^{-2}$, ensured the stability of Algorithm 3. Following the procedure detailed in Section 3.4.3, the exponentiation parameter for on-the-fly dynamic range enhancement of the database is $a = 10^3$.

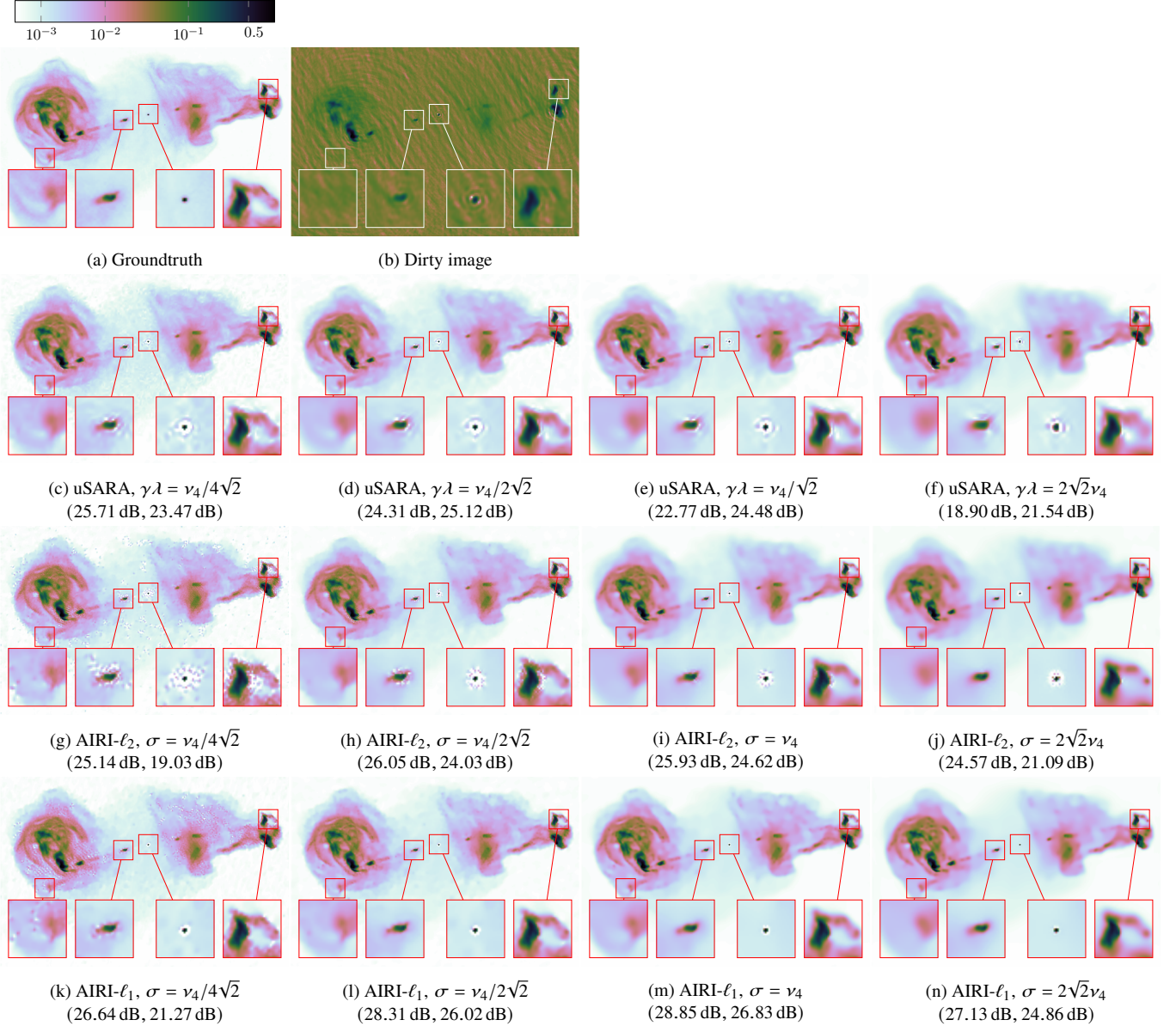


Figure 7. Experiment 2 results: Impact of the training noise level σ (resp. regularization parameter λ) in imaging with AIRI (resp. uSARA) on simulated RI data using 3c353 image as a groundtruth and the uv -pattern from Figure 5a ($\Delta T = 4$ h) in comparison with the reference value ν_4 suggested by the AIRI and uSARA heuristics. Top row: the groundtruth image 7a and the simulated dirty image 7b. Second row: estimated model images obtained with uSARA, with a regularization parameter λ increasing with the column index. Third (resp. fourth) row: estimated model images of AIRI- ℓ_2 (resp. AIRI- ℓ_1), with a training noise level σ increasing with the column index. Below each image we indicate the reconstruction metrics as (SNR, logSNR). All images are shown in logarithmic scale.

At the level of Algorithms 1, 2, and 3, the stepsize γ , convergence criteria $(\xi_i)_{1 \leq i \leq 3}$ and maximum number of iterations are set to the same values as in the previous experiment.

Finally, AIRI- ℓ_2 , AIRI- ℓ_1 , uSARA, and SARA are run in Matlab, except for CLEAN which is implemented in the highly optimized C++ WSClean package. uSARA, SARA, and CLEAN implementations utilise 10 CPU cores (Intel Xeon E5-2695 2.1 GHz). The parallel PDFB algorithmic structure underpinning SARA (see Section 2.3.1) optimizes the distribution of the operations involved at each iteration across those 10 CPU cores: 1 for the data-fidelity term, and 1 for each of the 9 bases of the average sparsity dictionary Ψ (Onose et al. 2016). For uSARA, the average sparsity dictionary is parallelized via a faceting procedure using 9 facets (Pruša 2012;

Thouvenin et al. 2021). AIRI- ℓ_2 and AIRI- ℓ_1 utilize 10 CPU cores and 1 GPU (NVIDIA Tesla V100). The latter is for the application of the denoiser, as commonly done with DNNs in deep learning. The DNN can be run on CPU, but this slows down the reconstructions significantly, as will be evident from the experimental results. Implementations of uSARA, SARA, and CLEAN leveraging GPUs are not investigated here.

4.4.2 Reconstruction quality

Figure 10 shows the average reconstruction SNR and logSNR as a function of the observation duration ΔT . Each point, on each of the two graphs, represents an average over 20 reconstructions arising



Figure 8. Experiment 2 results: Residual images associated with the reconstructions of Figure 7. Top row: residual images for the estimated model images obtained with uSARA, with a regularization parameter λ increasing with the column index. Second (resp. third) row: respective residual images for the estimated model images obtained with AIRI- ℓ_2 (resp. AIRI- ℓ_1), with a training noise level σ increasing with the column index. All images are shown in linear scale.

when considering the four test images in Figure 2 and five pointing directions, while error bars give the 95% confidence intervals. As expected, the reconstruction SNR increases with ΔT , as the data size increases with ΔT . The results extend the conclusion of the previous experiment of a superior performance of AIRI- ℓ_1 over both AIRI- ℓ_2 and uSARA across $\Delta T \in \{1 \text{ h}, 2 \text{ h}, 4 \text{ h}, 8 \text{ h}\}$. In SNR, AIRI- ℓ_1 and AIRI- ℓ_2 are respectively around 3dB and 2dB above uSARA. In logSNR, AIRI- ℓ_1 is between 1dB and 2dB above both AIRI- ℓ_2 and uSARA. The comparison with SARA reveals that AIRI- ℓ_1 is on par with SARA in SNR and slightly superior in logSNR across the range of measurement settings considered. As previously, we observe that the confidence interval around the mean SNR and logSNR values for both AIRI- ℓ_2 and AIRI- ℓ_1 is similar to that of uSARA and SARA, reflecting the robustness of the proposed method. The reconstruction quality of CLEAN is much inferior to those of AIRI and SARA approaches, for both SNR and logSNR and all measurement conditions considered.

We recall that SARA and uSARA leverage the same prior model, encapsulated in the averaged sparsity proximal operator. However, SARA relies on a constrained data-fidelity term (see SARA objective (6)), while uSARA uses an unconstrained formulation enforcing less abruptly data fidelity, in the sense that it imposes a soft penalty rather than a hard constraint (see uSARA objective (11)). A by-product of the present analysis is to confirm the superiority of the former over the latter.

Figure 13 shows the reconstructed Hercules A images for the considered methods and the uv -coverages shown in Figures 6a, 6b, and 6c. The visual analysis confirms the quantitative results from Fig-

ure 10. We acknowledge that the AIRI- ℓ_2 and AIRI- ℓ_1 algorithms can create artefacts by over-emphasising small structures (see the red zoom box in Figure 13m). SARA exhibits very similar quality to AIRI- ℓ_1 , but not always with the same resolution-to-artefacts tradeoff. The images suggest that the poor reconstruction of CLEAN stems from a strong offset in intensity values (see in particular the difference between the estimated higher intensity values in the upper rectangular zoom from Figures 13e, 13j, and 13o, and that of the groundtruth). Also note the important residual noise hiding low intensity features of the image, as well as remaining artefacts for $\Delta T = 1 \text{ h}$ and $\Delta T = 2 \text{ h}$.

4.4.3 Computational cost and reconstruction times

The computational costs for the various approaches considered are reported in Figure 11. Each point on the graphs is an average over the 20 simulated observations built from the four different groundtruths from Figure 2 and the five different uv -patterns shown in Figures 5 and 6c. Error bars show the 95% confidence intervals.

Figure 11a displays the average time per iteration, independently for each of the forward and backward steps of both uSARA and AIRI, as a function of the observation duration. We recall once more that uSARA relies on the same algorithmic structure as AIRI- ℓ_2 and AIRI- ℓ_1 . In both cases, the underpinning FB algorithm alternates between a (forward) gradient descent step enforcing data fidelity and a (backward) regularization step enforcing a prior model via the application of either the average sparsity proximal operator (uSARA, Algorithm 1) or a learned denoiser (AIRI, Algorithm 3). We note

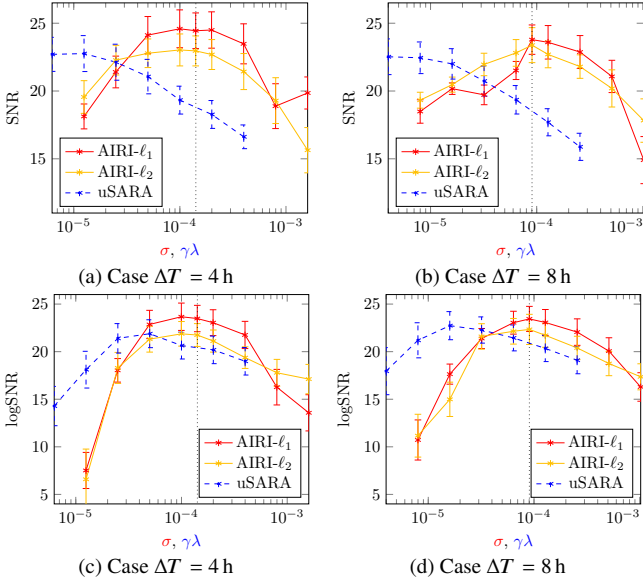


Figure 9. Experiment 2 results: Reconstruction metrics as a function of the training noise level σ in the case of AIRI- ℓ_2 and AIRI- ℓ_1 , or the thresholding parameter $\gamma\lambda$ in the case of uSARA. Top row: reconstruction SNR in the case of $\Delta T = 4$ h (a) and $\Delta T = 8$ h (b). Bottom row: reconstruction logSNR in the case of $\Delta T = 4$ h (c) and $\Delta T = 8$ h (d). Each point is an average over the 20 simulated observations built from the four different groundtruths from Figure 2 and the five different uv -patterns shown in Figures 5 and 6c. Error bars show the 95% confidence interval. On each graph, the black vertical dotted line indicates the common heuristic value for σ and $\gamma\lambda$ (i.e. v_4 for $\Delta T = 4$ h and v_8 for $\Delta T = 8$ h). Values for σ and $\gamma\lambda$ are sampled a factor $\sqrt{2}$ around the heuristic and by steps of 2 thereafter.

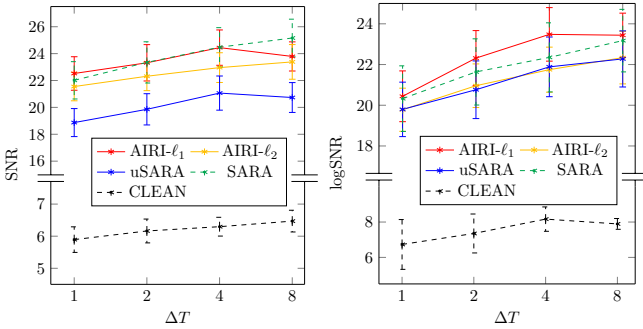


Figure 10. Experiment 3 results: Reconstruction SNR (left) and logSNR (right) as a function of the observation duration for AIRI- ℓ_2 , AIRI- ℓ_1 , uSARA, SARA, and CLEAN. Each point is an average over the 20 simulated observations built from the four different groundtruths from Figure 2 and the five different uv -patterns shown in Figures 5 and 6c. For AIRI- ℓ_2 and AIRI- ℓ_1 , σ is chosen at the heuristic. For uSARA, $\gamma\lambda$ is fine-tuned manually to optimize the logSNR, resulting in values between 3 and 6 times below the heuristic (in line with Figure 9). Error bars show the 95% confidence interval.

that, in such an algorithmic structure, the computational cost of the regularization step scales linearly with the image size, while that of the gradient descent step scales linearly with the data size.

Firstly, we observe from the figure that the computation time of the gradient step naturally scales linearly with the observation duration, which is indeed proportional to data size. Secondly, we acknowledge that the computation of the proximal operator within uSARA is slow, which is due to its sub-iterative nature. For the image and data sizes considered in our simulations, and given our CPU implementation, it always dominates the computation time of the gradient, on average

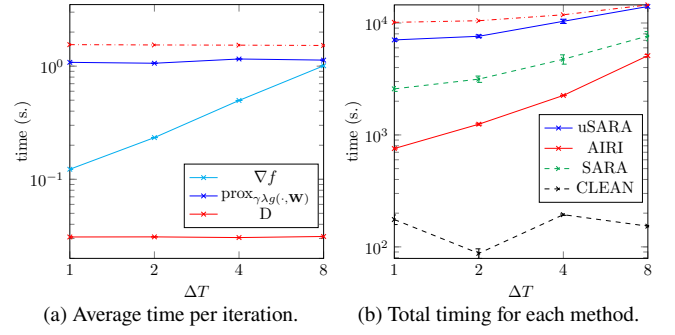


Figure 11. Experiment 3 results: Reconstruction times for AIRI- ℓ_2 , AIRI- ℓ_1 , uSARA, SARA, and CLEAN. AIRI- ℓ_2 and AIRI- ℓ_1 exhibit identical behaviours, with only AIRI- ℓ_2 results are reported and referred to as AIRI on the graphs. Each point is an average over the 20 simulated observations. Error bars show the (very small and virtually invisible) 95% confidence interval. For AIRI- ℓ_2 and AIRI- ℓ_1 , all reconstruction times are reported for both GPU (solid red lines) and CPU implementation (dashed red lines) of D. Left: average time per iteration in seconds (s) for the forward and backward operators involved in Algorithm 1 (∇f and $\text{prox}_{\gamma\lambda g}(\cdot, w)$) and Algorithm 3 (∇f and denoiser D), as a function of the observation duration. Right: average total reconstruction times for AIRI- ℓ_2 , AIRI- ℓ_1 , uSARA, SARA, and CLEAN, as a function of the observation duration.

per iteration of Algorithm 1. This conclusion holds despite the fact that we have carefully optimized the external parameters of Algorithm 1 and Algorithm 2 to optimize the reconstruction time (K in Algorithm 1, and the tolerance criterion ξ_2 and dual variable v_0 in Algorithm 2). In that regard, we note that an efficient initialization for the dual variable v_0 consists in setting it as the dual variable from the previous use of Algorithm 2. Using such an initialization, the number of sub-iterations for Algorithm 2 progressively decreases with the iteration count in Algorithm 1. Thirdly, using a standard GPU implementation of the AIRI- ℓ_2 and AIRI- ℓ_1 denoisers, their application is two orders of magnitude faster than the computation of the proximal operator. A CPU implementation of the denoisers makes them even slower than the proximal operator in uSARA. For the image and data sizes at stake, the AIRI denoisers on GPU are also significantly faster than the computation of the gradient, on average per iteration of Algorithm 1.

Figure 11b displays the total reconstruction times for uSARA and AIRI as a function of the observation duration, and in comparison with SARA and CLEAN. The AIRI- ℓ_2 and AIRI- ℓ_1 reconstruction times with denoiser on GPU scale almost linearly with the observation duration, due to the domination of the gradient step. For uSARA, and for AIRI- ℓ_2 and AIRI- ℓ_1 with denoiser on CPU, the dependency on observation duration is less severe given the domination of the regularization step at each iteration. Overall, given the speed up in the regularization step, the total reconstruction time of AIRI with denoiser on GPU is significantly (5 to 10 times) lower than the one of uSARA. AIRI- ℓ_2 and AIRI- ℓ_1 with denoiser on CPU are much slower, in fact slightly slower than uSARA itself. SARA offers reconstruction time between those of AIRI and uSARA. CLEAN remains significantly faster than AIRI (4 to 15 times).

To summarize, the application of an AIRI denoiser (on GPU) is orders of magnitude faster than that of the average sparsity proximal operator of uSARA (on CPU). Substituting the former by the latter does not only provide superior imaging quality, but significantly reduces the computational cost of the regularization step. For image and data sizes where the uSARA regularization step dominates over the gradient-descent data-fidelity step, a cost reduction in the former, substituting the proximal operator for a DNN denoiser leads to sig-

nificant speed up of the algorithm. In Figure 13, we also report the reconstruction times associated with the reconstructions. These are in line with the observations from Figure 11.

4.5 Experiment 4: validating AIRI at (larger) scale

4.5.1 Simulation setup

In this experiment, we validate AIRI- ℓ_2 and AIRI- ℓ_1 at larger image size, and for a higher dynamic range reconstruction, in comparison with uSARA, SARA, and CLEAN. As a groundtruth image, we consider a 2176×2176 -sized Cygnus A image observed at 5.035GHz with 10^5 dynamic range, taken from Thouvenin et al. (2021). RI data are simulated following the model (1), using the VLA uv -coverage displayed in Figure 12b at the wavelength 0.3m and using the configurations A and C of the VLA, which corresponds to a total observation duration of 7 h (resp. 10 h) for band A (resp. for band C), leading to a total of 972258 data points. The data are corrupted with a zero-mean random Gaussian noise resulting in $i\text{SNR} = 30\text{dB}$. Here again, we note that the uv -pattern extends to the edge of the considered Fourier domain, corresponding to reconstructing at, or just above, the nominal resolution of the observation.

Regarding Algorithms 1, 2, and 3, the stepsize γ , convergence criteria $(\xi_i)_{1 \leq i \leq 3}$, and maximum number of iterations are set to the same values as in the previous experiment. Since the image has a peak intensity value of about $\alpha = 0.922$, the inverse problem solved via the AIRI approach is rescaled according to (21). The AIRI- ℓ_2 and AIRI- ℓ_1 denoisers are trained with the training noise level σ set at the proposed heuristic (22), yielding $\sigma = 1.4 \times 10^{-5}$. As usual, the values of κ in the training loss are optimized to enforce stability of Algorithm 3, with the safety margin parameter as usual set to $\varepsilon = 5 \times 10^{-2}$. Interestingly, the resulting values are similar to those for training at lower dynamic range in the previous experiments: $\kappa = 10^{-9}$ for AIRI- ℓ_2 and $\kappa = 5 \times 10^{-6}$ for AIRI- ℓ_1 . Following the procedure detailed in Section 3.4.3, the corresponding exponentiation parameter for on-the-fly dynamic range enhancement of the database is $a = 1.1 \times 10^4$. For uSARA, the optimal value of λ is, as before, fine-tuned manually to optimize the logSNR of each reconstruction. The resulting soft-thresholding value is nearly 3 times below the reference (23), right on the $1/3$ -corrected value, at $\gamma\lambda = 5 \times 10^{-6}$.

4.5.2 Experimental results

Reconstruction results of the different approaches are shown in Figure 12. More precisely, estimated model images, overlaid with zooms on key regions of the radio galaxy, are provided in logarithmic scale, together with the groundtruth image, the VLA uv -pattern, and the dirty image. All in all, the results show that the AIRI approach does scale to larger image sizes and dynamic ranges. In terms of imaging quality, both a visual analysis and the metrics show that SARA offers the best results, closely followed by AIRI- ℓ_1 , AIRI- ℓ_2 , and uSARA, all strongly improving over CLEAN. In terms of computation time, CLEAN is still significantly faster than AIRI- ℓ_1 and AIRI- ℓ_2 , which however confirms the expected acceleration potential over SARA and uSARA. We discuss these results in more details in what follows.

Firstly, when comparing AIRI- ℓ_1 and AIRI- ℓ_2 to uSARA, the visual analysis confirms the results of the previous experiments, with AIRI- ℓ_2 producing a smoother reconstruction than uSARA but with less artefacts, while AIRI- ℓ_1 preserves the resolution offered by uSARA, further reducing artefacts compared to AIRI- ℓ_2 . However, numerically, if AIRI- ℓ_1 and AIRI- ℓ_2 still provide better SNR values than uSARA, they both yield slightly lower logSNR values, unlike what

was observed in the previous experiments. These numbers indicate a better performance of AIRI- ℓ_1 and AIRI- ℓ_2 to recover high-intensity signal (see red and blue zoom boxes), while uSARA performs slightly better at recovering faint emission (see grey zoom box).

Secondly, SARA outperforms AIRI- ℓ_1 , AIRI- ℓ_2 , and uSARA by a large margin in SNR, but also to a lesser extent in logSNR, and in terms of visible resolution and ability to recover faint emission. Note that the large SNR discrepancy (versus logSNR and overall visual reconstruction quality) is largely related to the difficulty of AIRI- ℓ_1 , AIRI- ℓ_2 , and uSARA to recover the brightest compact source situated at the centre of the image (see the central rectangular zoom), corresponding to the central black hole of the radio galaxy. In order to measure the reconstruction quality of the rest of the field of view, we introduce the SNR_{mask} metric, corresponding to the regular SNR evaluated on the images after masking of a 10×10 pixels region centered on the brightest compact source. The much higher values of SNR_{mask} obtained by AIRI- ℓ_1 , AIRI- ℓ_2 , and uSARA indicate the bias of the SNR metric towards the brightest emission in the field of view. That said, the superiority of SARA over uSARA was already acknowledged in Section 4.4, and attributed to the fact that uSARA uses an unconstrained formulation enforcing less abruptly data fidelity. While in the previous experiments the superior prior model encapsulated in the AIRI- ℓ_1 denoiser, and to a lesser extent the AIRI- ℓ_2 denoiser, compensated for the suboptimality of the unconstrained formulation that they share with uSARA, they also appear to struggle in the more challenging case of Cygnus A. Last but not least, we mention that the target groundtruth image was originally reconstructed with a SARA-based approach for joint calibration and imaging (Repetti et al. 2017; Dabbech et al. 2021), which may possibly slightly bias the results towards SARA itself.

Finally, one can see at first glance the limited dynamic range of the CLEAN image and the loss of resolution compared to all other methods, leading to much inferior SNR and logSNR values. CLEAN was however approximately 10 times faster than AIRI- ℓ_1 and AIRI- ℓ_2 , themselves approximately 4 and 5 times faster than SARA and uSARA respectively.

5 CONCLUSION & FUTURE WORK

5.1 Conclusion for both AIRI & uSARA

In this work, we have proposed a new algorithmic framework for scalable precision RI imaging, dubbed AIRI. The approach consists in encapsulating a prior image model in a DNN denoiser, and plugging it in lieu of the proximal regularization operator of an optimization algorithm of the SARA family for image reconstruction. AIRI inherits the robustness and interpretability of optimization approaches and the learning power and speed of networks, while avoiding generalizability limitations of end-to-end networks, for which training involves the details of the measurement model.

More specifically, we have firstly designed a realistic low dynamic range training database from optical images. We have also established a method to train firmly nonexpansive denoisers at a noise level inferred from the target dynamic ranges of reconstruction, with either an ℓ_2 or ℓ_1 loss, including a procedure for on-the-fly database dynamic range enhancement. Finally, the AIRI- ℓ_2 and AIRI- ℓ_1 algorithms resulting from plugging the denoisers into the FB algorithm were validated in simulation for reconstruction of images involving complex structure with diffuse and faint emission across the field of view (image sizes up to 2176×2176 and dynamic range up to 10^5). The benchmark algorithms included CLEAN, the state-of-the-art

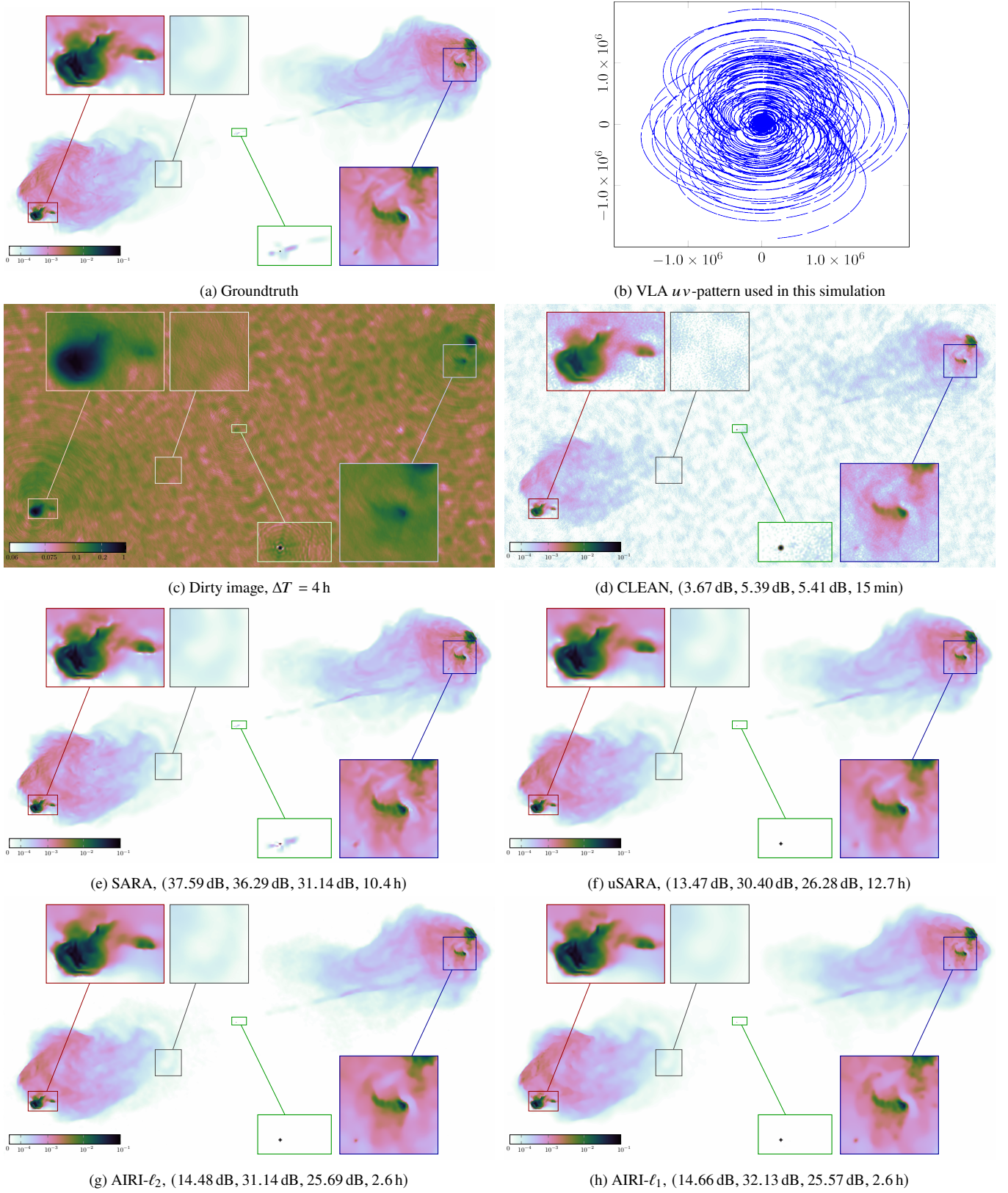


Figure 12. Experiment 4 results: Reconstruction results of the different algorithms for simulated RI data on the Cygnus A image of size $n = 2176 \times 2176$ with a VLA uv -pattern. First row: 12a shows the groundtruth, while 12b shows the uv -pattern. Second row: 12c shows the dirty image, and 12d shows the CLEAN reconstruction. Third row: 12e shows the SARA reconstruction, while 12f shows the uSARA reconstruction. Fourth row: 12g and 12h show the AIRI- ℓ_2 and AIRI- ℓ_1 reconstructions respectively. Below each image we indicate the reconstruction metrics and time as (SNR, SNR_{mask}, logSNR, reconstruction time); the SNR_{mask} metric corresponds to the SNR where the 10 central pixels in the image have been masked. All images are shown in logarithmic scale; for clarity, the colourbar is saturated at 10^{-1} .

SARA algorithm, as well as its new unconstrained version uSARA, which only differs from AIRI- ℓ_2 and AIRI- ℓ_1 by the use of the average sparsity proximal regularization operator instead of a learned denoiser in the FB algorithm.

Our results show that the first incarnations of AIRI are already competitive with, if not superior to, the advanced optimization algorithms of the SARA family in imaging quality, well beyond the capability of CLEAN. With regards to computation time, the AIRI approach was shown to provide a significant acceleration potential over uSARA and SARA, thanks to the inference speed of DNN denoisers over the averaged sparsity proximal operator, but remain significantly slower than CLEAN. The results also confirm the validity of our heuristic to set the training noise level σ , consisting in enforcing equality of the training and target dynamic range of reconstruction, and the validity of the database exponentiation approach (with parameter a), consisting in enforcing equality of the final nominal dynamic range of the database and target dynamic range of reconstruction. This provides a significant advantage over uSARA, for which the regularization parameter λ requires manual fine-tuning, even though the fact that the corresponding heuristic (and its 1/3-corrected version) provides an appropriate reference upper-bound for the optimal value is an interesting result. In this context, a fully fledged AIRI package universally applicable for all RI measurement settings would simply require training, once and for all, a one-dimensional σ -shelf of denoisers extending across the segment of dynamic ranges of interest. Users would simply have to select the appropriate denoiser from the shelf before running a reconstruction.

5.2 Current limitations & future work

In what follows, we discuss current limitations of the AIRI framework, and future work. This also includes considerations for further developments of uSARA, which, we emphasize, was never proposed before as a standalone RI imaging algorithm. Firstly, the modified DnCNN denoiser architecture used, the ℓ_2 and ℓ_1 losses considered, as well as the set of optical images used to build a training database constitute the most basic choices leading to our first AIRI- ℓ_2 and AIRI- ℓ_1 incarnations of the framework. We anticipate that future work, building a richer database from RI observation, and considering more advanced losses (such as adversarial losses, Wang et al. 2018a) and network architectures (such as Unets, Hurault et al. 2022), can provide a quantum jump in imaging precision with AIRI. We also acknowledge that our approach to enforce the firm nonexpansiveness of the denoiser is only approximate, and relies on fine-tuning the regularization parameter κ in the training loss. Simpler and more precise approaches to ensure firm nonexpansiveness should be investigated in the future (e.g. leveraging 1-Lipschitz layers). We note however that the proposed approach provides in practice a robust way to ensure convergence of the resulting PnP algorithms. Also, interestingly, across our experiments, the optimized values of κ were found to be independent of the training conditions (i.e. the same value apply independently of σ and a), only effectively depending on the choice of loss (ℓ_2 or ℓ_1). Moreover, we emphasize that, in the σ -shelf approach, denoisers ought to be trained once and for all across the segment of dynamic ranges of interest, and not for each target reconstruction, so that fine-tuning a regularization parameter is not a major problem.

Secondly, an approach enabling training a single denoiser applicable for all dynamic ranges (as opposed to the currently proposed one-dimensional σ -shelf based on the heuristic) would further simplify AIRI and should be contemplated (Zhang et al. 2021).

Thirdly, fully optimized and parallelized implementations of AIRI algorithms, but also SARA, or uSARA, leveraging GPUs not only

for DNN denoisers, but also for the implementation of the linear (measurement or regularization) operators involved, should be investigated. This should lead to further acceleration of these approaches, and possibly participate to closing the gap with CLEAN in terms of reconstruction time. We also note that accelerated versions of uSARA are achievable, in particular leveraging preconditioning strategies (Repetti & Wiaux 2021).

Finally, with regards to the details of the target imaging modality, we have investigated monochromatic intensity imaging on small fields of view only, with mild, if any, super-resolution factor with respect to the nominal resolution of the observation, as set by the largest baseline. Extensions of the framework to further super-resolution functionality and to wideband polarization imaging on wide fields of view (in particular including w -terms in the measurement operator) should be contemplated. Also, a by-product of the present analysis is to confirm the superiority of SARA over uSARA, due to the constrained approach to data fidelity in SARA, versus the unconstrained approach underpinning uSARA. In this context, the superior results of AIRI over uSARA are entirely related to the capability to encapsulate a better prior model than the average sparsity model in learned DNN denoisers. On the one hand, a first possible enhancement of the AIRI approach would consist in developing a PnP version of SARA (as opposed to uSARA), simultaneously taking advantage of networks to learn prior models and of the constrained data-fidelity formulation. On the other hand, to date, the unconstrained formulation underpinning uSARA, AIRI- ℓ_2 , and AIRI- ℓ_1 is a critical building block of the only joint optimization-based algorithm proposed for RI capable of handling jointly DDE calibration and imaging (Repetti et al. 2017; Dabbech et al. 2021). This is a strong justification for the study of unconstrained versus constrained formulations of the imaging module. Tailoring AIRI denoisers for a PnP version of SARA for pure imaging, or for joint DDE calibration and imaging, are important directions for future work.

ACKNOWLEDGEMENTS

The research of M. T. was funded by Heriot-Watt under the James Watt Scholarship scheme. The work of M. T., A. D., and Y. W. was supported by EPSRC under grant EP/T028270/1. The computing resources came from the Cirrus UK National Tier-2 HPC Service at EPCC (<http://www.cirrus.ac.uk>) funded by the University of Edinburgh and EPSRC (EP/P020267/1), partly through time allocation under the SUSAN project, and partly through GPU resources directly provided by EPCC (Adrian Jackson). Credits for the 32 images used in our training database go to NOIRLab/NSF/AURA/H. Schweiker/WIYN/T.A. Rector (University of Alaska Anchorage). The radio images were taken from: for Hercules A: R. Perley and W. Cotton (NRAO/AUI/NSF), for 3c353: NRAO/VLA, for Centaurus A: NRAO/AUI/NSF/Univ.Hertfordshire/M.Hardcastle.

DATA AVAILABILITY

AIRI code will be made available as part of the planned release of and joint parallel toolbox for AIRI and uSARA.

REFERENCES

Abdulaziz A., Dabbech A., Onose A., Wiaux Y., 2016, in European Signal Processing Conf., pp 388–392

- Abdulaziz A., Dabbech A., Wiaux Y., 2019, MNRAS, 489, 1230
- Adler J., Öktem O., 2018, IEEE Transactions on Medical Imaging, 37, 1322
- Ahmad R., Bouman C. A., Buzzard G. T., Chan S., Liu S., Reehorst E. T., Schniter P., 2020, IEEE Signal Processing Magazine, 37, 105
- Arras P., Knollr Müller J., Junklewitz H., Enßlin T. A., 2018, in European Signal Processing Conf.. pp 2683–2687
- Arras P., Frank P., Leike R., Westermann R., Enßlin T. A., 2019, A&A, 627, A134
- Attouch H., Bolte J., Svaiter B. F., 2013, Math. Programming, 137, 91
- Balestrieri R., Baraniuk R., 2021, arXiv preprint arXiv:2104.00219
- Baraniuk R. G., 2007, IEEE Signal Processing Magazine, 24, 118
- Bauschke H. H., Combettes P. L., 2017, Convex analysis and monotone operator theory in Hilbert spaces. Springer
- Beck A., Teboulle M., 2009, SIAM J. on Imaging Sci., 2, 183
- Bertocchi C., Chouzenoux E., Corbineau M.-C., Pesquet J.-C., Prato M., 2020, Inverse Problems, 36, 034005
- Bhatnagar S., Cornwell T., 2004, A&A, 426, 747
- Birdi J., Repetti A., Wiaux Y., 2018, MNRAS, 478, 4442
- Birdi J., Repetti A., Wiaux Y., 2020, MNRAS, 492, 3509
- Bonaldi A., Braun R., 2018, arXiv preprint arXiv:1811.10454
- Bonettini S., Zanella R., Zanni L., 2008, Inverse problems, 25, 015002
- Boyd S., Parikh N., Chu E., 2011, Distributed optimization and statistical learning via the alternating direction method of multipliers. Now Publishers Inc
- Bredies K., Holler M., 2020, Inverse Problems, 36, 123001
- Bredies K., Kunisch K., Pock T., 2010, SIAM J. on Imaging Sci., 3, 492
- Briggs D. S., 1995, in American Astron. Soc. Meeting Abstracts. p. 112.02
- Bryan G. L., et al., 2014, ApJS, 211, 19
- Buades A., Coll B., Morel J.-M., 2011, Image Processing On Line, 1, 208
- Cai X., Pereyra M., McEwen J. D., 2018, MNRAS, 480, 4154
- Candes E., Demanet L., 2003, Comptes Rendus Mathématique, 336, 395
- Candès E. J., Romberg J., Tao T., 2006, IEEE Trans. on Inf. Theor., 52, 489
- Candès E. J., Wakin M. B., Boyd S. P., 2008, J. of Fourier analysis and applications, 14, 877
- Carrillo R. E., McEwen J. D., Wiaux Y., 2012, MNRAS, 426, 1223
- Carrillo R. E., McEwen J. D., Wiaux Y., 2014, MNRAS, 439, 3591
- Chambolle A., Pock T., 2011, J. of Math. Imaging and Vision, 40, 120
- Chambolle A., De Vore R. A., Lee N.-Y., Lucier B. J., 1998, IEEE Trans. on Image Processing, 7, 319
- Chan S. H., Wang X., Elgendy O. A., 2016, IEEE Trans. on Comput. Imaging, 3, 84
- Chouzenoux E., Pesquet J.-C., Repetti A., 2014, J. of Optimization Theor. and Applications, 162, 107
- Cohen R., Elad M., Milanfar P., 2021, SIAM J. on Imaging Sci., 14, 1374
- Combettes P. L., Pesquet J.-C., 2011, in , Fixed-point algorithms for inverse problems in science and engineering. Springer, pp 185–212
- Combettes P. L., Pesquet J.-C., 2015, SIAM Journal on Optimization, 25, 1221
- Combettes P. L., Wajs V. R., 2005, Multiscale Modeling & Simulation, 4, 1168
- Connor L., Bouman K. L., Ravi V., Hallinan G., 2021, arXiv preprint arXiv:2111.03249
- Cornwell T. J., Golap K., Bhatnagar S., 2008, IEEE J. of Selected Topics in Signal Processing, 2, 647
- Dabbech A., Ferrari C., Mary D., Slezak E., Smirnov O., Kenyon J. S., 2015, A&A, 576, A7
- Dabbech A., Onose A., Abdulaziz A., Perley R. A., Smirnov O. M., Wiaux Y., 2018, MNRAS, 476, 2853
- Dabbech A., Repetti A., Perley R. A., Smirnov O. M., Wiaux Y., 2021, arXiv preprint arXiv:2102.00065
- Dabov K., Foi A., Katkovnik V., Egiazarian K., 2007, IEEE Trans. on Image Processing, 16, 2080
- Do M. N., Vetterli M., 2003, in , Vol. 10, Studies in Comp. Math.. Elsevier, pp 83–105
- Donoho D. L., 2006, IEEE Trans. on Inf. Theor., 52, 1289
- Donoho D. L., Johnstone I. M., 1995, J. of the American Statistical Association, 90, 1200
- Eckstein J., Bertsekas D. P., 1992, Math. Programming, 55, 293
- Fessler J. A., 2020, IEEE Signal Processing Magazine, 37, 33
- Garsden H., et al., 2015, A&A, 575, A90
- Gheller C., Vazza F., 2021, MNRAS
- Golub G. H., Van Loan C. F., 2013, Matrix computations. JHU press
- Gregor K., LeCun Y., 2010, in Int. Conf. on Machine Learning. pp 399–406
- Guan S., Khan A. A., Sikdar S., Chitnis P. V., 2019, IEEE J. of Biomedical and Health Inf., 24, 568
- Gupta H., Jin K. H., Nguyen H. Q., McCann M. T., Unser M., 2018, IEEE Trans. on Medical Imaging, 37, 1440
- Hertrich J., Neumayer S., Steidl G., 2021, Linear Algebra and its Applications, 631, 203
- Högbom J., 1974, A&AS, 15, 417
- Hurault S., Leclaire A., Papadakis N., 2022, arXiv preprint arXiv:2201.13256
- Ian J Goodfellow J. S., Szegedy C., 2015, in Int. Conf. on Learning Representations.
- Jin K. H., McCann M. T., Froustey E., Unser M., 2017, IEEE Trans. on Image Processing, 26, 4509
- Jonas J., et al., 2018, in MeerKAT Sci.: On the Pathway to the SKA. p. 001
- Junklewitz H., Bell M., Enßlin T., 2015, A&A, 581, A59
- Kingma D. P., Ba J., 2015, in International Conference on Learning Representations.
- Levin A., Weiss Y., Durand F., Freeman W. T., 2009, in 2009 IEEE Conf. on Comput. Vision and Pattern Recognition. pp 1964–1971
- Li F., Cornwell T. J., de Hoog F., 2011, A&A, 528, A31
- Luisier F., Blu T., Unser M., 2007, IEEE Trans. on Image Processing, 16, 593
- Lustig M., Donoho D., Pauly J. M., 2007, Magn. Resonance in Medicine, 58, 1182
- Maddox W., Tang S., Moreno P., Wilson A. G., Damianou A., 2021, in International Conference on Artificial Intelligence and Statistics. pp 2737–2745
- Mairal J., Bach F., Ponce J., Sapiro G., 2009, in Int. Conf. on Machine Learning. pp 689–696
- Majumdar A., Ward R. K., 2012, Magnetic resonance imaging, 30, 1032
- Mallat S., 1999, A wavelet tour of signal processing. Elsevier
- Muckley M. J., et al., 2021, IEEE Trans. on Medical Imaging, 40, 2306
- Needell D., Ward R., 2013, SIAM J. on Imaging Sci., 6, 1035
- Nguyen A., Yosinski J., Clune J., 2015, in IEEE Conf. on Comput. Vision and Pattern Recognition. pp 427–436
- Offringa A., et al., 2014, MNRAS, 444, 606
- Ongie G., Jalal A., Metzler C. A., Baraniuk R. G., Dimakis A. G., Willett R., 2020, IEEE J. on Selected Areas in Inf. Theor., 1, 39
- Onose A., Carrillo R. E., Repetti A., McEwen J. D., Thiran J.-P., Pesquet J.-C., Wiaux Y., 2016, MNRAS, 462, 4314
- Onose A., Dabbech A., Wiaux Y., 2017, MNRAS, 469, 938
- Pang T., Du C., Dong Y., Zhu J., 2018, Advances in Neural Inf. Processing Syst., 31
- Paszke A., et al., 2017, in Advances in Neural Inf. Processing Syst. Workshop.
- Pesquet J.-C., Repetti A., 2014, arXiv preprint arXiv:1406.6404
- Pesquet J.-C., Repetti A., Terris M., Wiaux Y., 2021, SIAM J. on Imaging Sci., 14, 1206
- Poon C., 2015, SIAM J. on Imaging Sci., 8, 682
- Pratley L., McEwen J. D., d’Avezac M., Carrillo R. E., Onose A., Wiaux Y., 2018, MNRAS, 473, 1038
- Pruša Z., 2012, PhD thesis, Brno university of technology
- Puri-Psi 2021, Puri-Psi: Parallel Proximal Scalable Imaging, BASP group, <https://basp-group.github.io/Puri-Psi/>
- Repetti A., Wiaux Y., 2021, SIAM J. on Optimization, 31, 1215
- Repetti A., Birdi J., Dabbech A., Wiaux Y., 2017, MNRAS, 470, 3981
- Repetti A., Pereyra M., Wiaux Y., 2018, in European Signal Processing Conf.. pp 2668–2672
- Repetti A., Pereyra M., Wiaux Y., 2019, SIAM J. on Imaging Sci., 12, 87
- Romano Y., Elad M., Milanfar P., 2017, SIAM J. on Imaging Sci., 10, 1804
- Rudin L. I., Osher S., Fatemi E., 1992, Phys. D: nonlinear phenomena, 60, 259
- Ryu E., Liu J., Wang S., Chen X., Wang Z., Yin W., 2019, in Int. Conf. on Machine Learning. pp 5546–5557
- Scaman K., Virmaux A., 2018, arXiv preprint arXiv:1805.10965
- Schwab F. R., Cotton W. D., 1983, AJ, 88, 688
- Schwarz U., 1978, A&A, 65, 345

- Selesnick I. W., Baraniuk R. G., Kingsbury N. C., 2005, *IEEE Signal Processing Magazine*, 22, 123
- Sun H., Bouman K. L., 2020, arXiv preprint arXiv:2010.14462, 9
- Terris M., Abdulaziz A., Dabbech A., Jiang M., Repetti A., Pesquet J.-C., Wiaux Y., 2019, in *SPARS workshop*.
- Terris M., Repetti A., Pesquet J.-C., Wiaux Y., 2020, in *IEEE Int. Conf. on Acoustics, Speech and Signal Processing*. pp 8658–8662
- Terris M., Repetti A., Pesquet J.-C., Wiaux Y., 2021, in *IEEE Int. Conf. on Image Processing*. pp 1684–1688
- Thompson A. R., Moran J. M., Swenson Jr G. W., 2017, *Interferometry and synthesis in radio astronomy*. Springer Nat.
- Thouvenin P.-A., Abdulaziz A., Dabbech A., Repetti A., Wiaux Y., 2021, *MNRAS*
- Venkatakrisnan S. V., Bouman C. A., Wohlberg B., 2013, in *2013 IEEE Global Conf. on Signal and Inf. Processing*. pp 945–948
- Vidal A. F., De Bortoli V., Pereyra M., Durmus A., 2020, *SIAM J. on Imaging Sci.*, 13, 1945
- Wang L., Xiong Z., Gao D., Shi G., Wu F., 2015, *Applied optics*, 54, 848
- Wang X., Yu K., Wu S., Gu J., Liu Y., Dong C., Qiao Y., Change Loy C., 2018a, in *European Conf. on Comput. Vision Workshops*. pp 0–0
- Wang G., Ye J. C., Mueller K., Fessler J. A., 2018b, *IEEE Trans. on Medical Imaging*, 37, 1289
- Wiaux Y., Jacques L., Puy G., Scaife A. M., Vandergheynst P., 2009, *MNRAS*, 395, 1733
- Xie Q., Zhou M., Zhao Q., Meng D., Zuo W., Xu Z., 2019, in *IEEE/CVF Conf. on Comput. Vision and Pattern Recognition*. pp 1585–1594
- Yang J., Wright J., Huang T. S., Ma Y., 2010, *IEEE Trans. on Image Processing*, 19, 2861
- Zbontar J., et al., 2018, arXiv preprint arXiv:1811.08839
- Zhang K., Zuo W., Chen Y., Meng D., Zhang L., 2017, *IEEE Trans. on Image Processing*, 26, 3142
- Zhang X., Yang W., Hu Y., Liu J., 2018, in *IEEE Int. Conf. on Image Processing*. pp 390–394
- Zhang Y., Li K., Li K., Zhong B., Fu Y., 2019a, arXiv preprint arXiv:1903.10082
- Zhang K., Zuo W., Zhang L., 2019b, in *IEEE/CVF Conf. on Comput. Vision and Pattern Recognition*. pp 1671–1681
- Zhang K., Li Y., Zuo W., Zhang L., Van Gool L., Timofte R., 2021, *IEEE Trans. on Pattern Analysis and Machine Intelligence*
- Zhou Y., Jiao J., Huang H., Wang Y., Wang J., Shi H., Huang T., 2020, in *AAAI Conf. on Artificial Intelligence*. pp 13074–13081

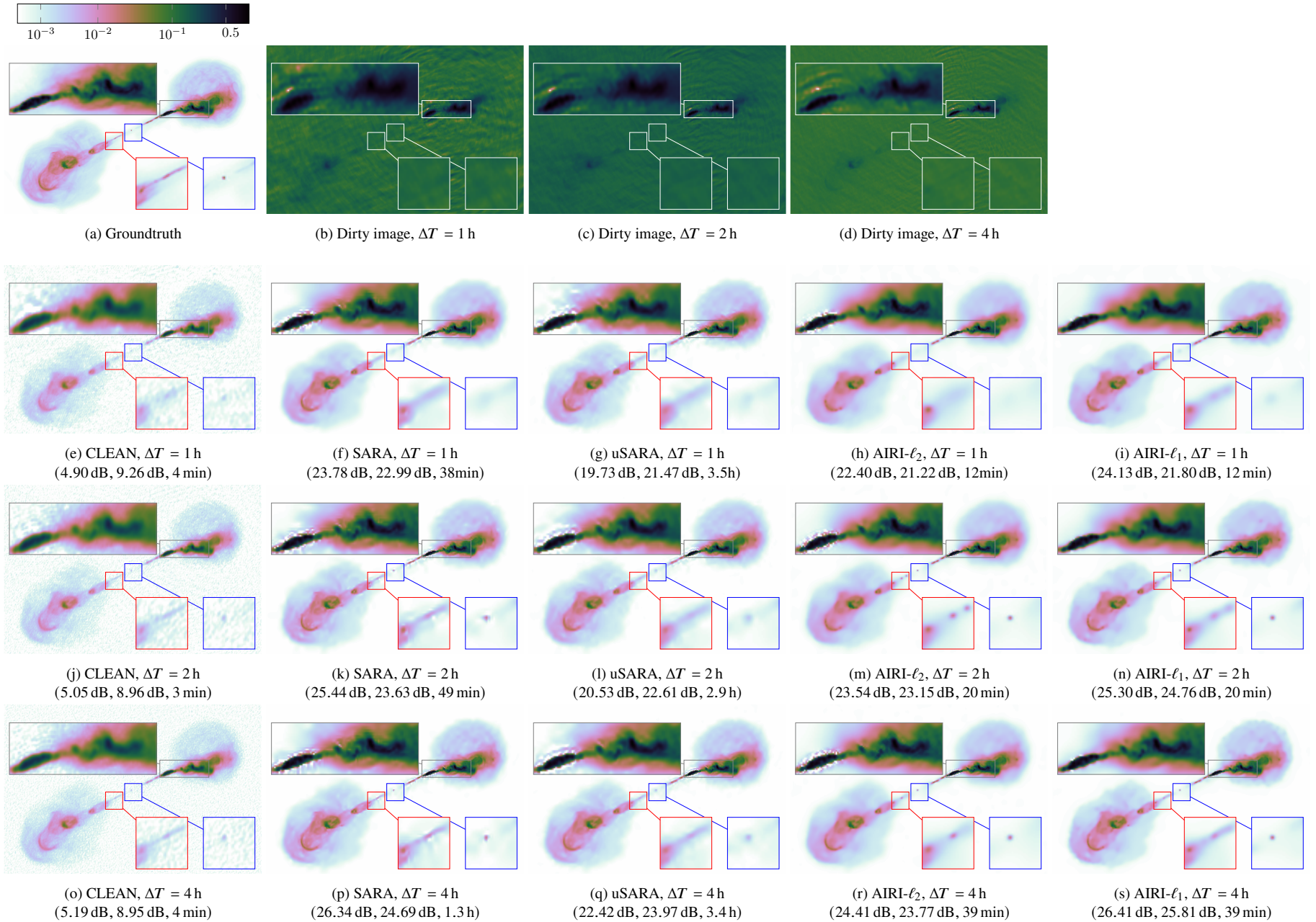


Figure 13. Experiment 3 results: Influence of the observation duration ΔT on the reconstruction quality for the different algorithms with the pointing position from Figure 6; the associated uv -patterns are displayed in Figures 6a, 6b, and 6c. Second, third and last row show reconstruction results for $\Delta T = 1$ h, $\Delta T = 2$ h and $\Delta T = 4$ h, respectively. For these three rows, each column from left to right shows estimated model images obtained with CLEAN, SARA, uSARA, AIRI- ℓ_2 , and AIRI- ℓ_1 , respectively. Below each reconstruction we indicate the reconstruction metrics and time (SNR, logSNR, reconstruction time). All images are shown in logarithmic scale.

This paper has been typeset from a $\text{\TeX}/\text{\LaTeX}$ file prepared by the author.